J. Fluid Mech. (2002), *vol.* 464, *pp.* 311–344.
DOI: 10.1017/S002211200200887X Printed in the United Kingdom

Flow transitions in three-dimensional double-diffusive fingering convection in a porous cavity

By I. SEZAI

Department of Mechanical Engineering, Eastern Mediterranean University, Magosa, Mersin 10, Turkey

(Received 13 June 2000 and in revised form 15 January 2002)

In the present study the existence of multiple three-dimensional double-diffusive flow patterns in a horizontal rectangular porous cavity of a square cross-section, having horizontal aspect ratios $A_x = A_y = 2$ is investigated numerically. Opposing vertical gradients of temperature and concentration are applied between the two horizontal walls of the cavity, where the solute gradient is destabilizing against a stabilizing temperature gradient. All vertical walls are considered to be impermeable and adiabatic. The Brinkman and Forchheimer terms are included in the momentum equations where the convective terms are retained. The effect of the buoyancy ratio, N, thermal Rayleigh number, Ra_T and Lewis number, Le, on the formation of multiple flow patterns is investigated over a wide range of parameters. Altogether 36 symmetric flow structures have been identified when each of the parameters N, Ra_T, and Le is varied independently, keeping the others as constants. The results of the calculations are presented in terms of the average Sherwood number curves consisting of different solution branches, where transitions between the branches are indicated. The flow patterns are classified according to their symmetry properties and the type of symmetries broken or preserved are identified during the bifurcation processes.

1. Introduction

Fluid flow in porous media resulting from the double diffusive effects of temperature and concentration gradients has been the subject of intensive study because of its importance in the prediction of groundwater contamination in aquifers, waste and fertilizer migration in saturated soil, moisture movement through air contained in fibrous insulations and solute transfer in the mushy layer during the solidification of binary alloys.

Double-diffusive convection in a fluid layer with vertical temperature and concentration gradients can be broadly categorized as 'fingering' or 'diffusive'. When the faster diffusing component is stabilizing to the vertical density gradient the system is in the fingering regime. When the slower diffusing component is stabilizing and the faster diffusing component destabilizing, the system is in the diffusive regime. The case of warm salty ground water overlying cold fresh water is an example where salt fingers can form. Salt fingers transport solute very efficiently vertically and may be responsible for the contamination of groundwater reservoirs (Imhoff & Green 1988). Another example of fingering convection is encountered during the solidification of binary alloys when the mould is cooled from below (Worster

1986; Emms & Fowler 1994; Anderson & Worster 1995). As the binary alloy solidifies there is rejection of one or other of the components into the melt since such mixtures do not have a single temperature at which a change of phase occurs, as can be observed from the solidus and liquidus curves of the phase diagram. The result is a mushy layer, separating the liquid and solid phases, which can be considered as a porous medium. If the rejected component is lighter, it will tend to form a concentration gradient, which will tend to destabilize the density gradient while the temperature gradient is stabilizing. If the thermal diffusivity is larger than the mass diffusivity the resulting double-diffusive convection is of the fingering type.

However, despite its importance, double-diffusive convection in the fingering regime in porous media has attracted much less attention than its counterpart in the diffusive regime. Much of the published work regarding double-diffusive convection in porous media with vertical concentration and density gradients concerns linear stability analysis. The stability of a horizontal porous layer saturated with a fluid having a stabilizing solute gradient, which is opposed by a destabilizing thermal gradient (diffusive regime) was first studied by Nield (1968). Using linear stability analysis he found that the critical value of the porous thermal Rayleigh number for the onset of convection is related to the solutal Rayleigh number. An extension of the analysis of Nield to the fingering regime was carried out by Taunton & Lightfoot (1972). Rubin (1973) has extended Nield's analysis to nonlinear salinity profiles. The effect of such salinity profiles on marginal stability and overstability, as well as on thermal convection, was investigated. Turbulent effects were included in a later analysis (Rubin 1976) to investigate the contamination of groundwater by saline water in aquifers. The effects of cross-diffusion produced by simultaneous interference of two transport processes, e.g. Soret and Dufour effects, on the stability of double-diffusive convection in a horizontal porous fluid layer bounded by two rigid boundaries were investigated by Patil & Rudriah (1980), Taslim & Narusawa (1986) and Rudraiah & Malashetty (1986).

Heat and mass transfer from a horizontal porous layer heated from below was investigated numerically by Trevisan & Bejan (1987) in the Darcy regime, where the effects of concentration on the buoyancy were neglected. The scaling laws of the overall mass transfer rate of the single-cell flow were also determined through a scaling analysis in the high-Rayleigh-number range. Double-diffusive convection in a porous square cavity heated from below with opposing vertical temperature and concentration gradients was investigated numerically by Rosenberg & Spera (1992) in the diffusive regime for a variety of initial salinity and boundary conditions. It was shown that flow dynamics depend strongly on buoyancy ratio. A mixed finite-difference and Galerkin method is used by Chen & Chen (1993) to study the double-diffusive convection in a horizontal porous layer in the fingering regime. The Darcy equation, including Brinkman and Forchheimer terms, was used for the momentum equations. The range of parameters in which the flow is steady, periodic or unsteady has been identified in terms of the porous thermal and solutal Rayleigh numbers.

Anisotropic thermoconvective effects in the double-diffusive convection in porous media with vertical temperature and concentration gradients were also studied. The effect of anisotropy of the porous layer on the marginal stability and on the initiation of salt fingers was studied by Tyvand (1980). It has been found that anisotropy may or may not favour salt fingers depending on a dimensionless diffusion parameter $r = (\alpha_1/D_1)/(\alpha_3/D_3)$, where α_1/D_1 is the effective thermal diffusivity/solutal diffusivity ratio of the porous medium in the horizontal direction and α_3/D_3 is the corresponding

ratio in the vertical direction. Anisotropy favours salt fingers if $r > 1$. Using a linear stability analysis Malashetty (1993) determined the effect of anisotropic thermoconvective currents on the critical Rayleigh number for both marginal and overstable motions in a horizontal porous layer saturated with a binary mixture. The purpose of the study of Zhao, Mülhaus & Hobbs (1998) was the investigation of the effect of geological inhomogeneity on the steady state heat and mineral transfer where a fluid saturated medium, heated from below, was used as a model. It has been found that inhomogeneity in permeability and thermal conductivity effects the pore–fluid convective flow significantly.

A linear stability analysis was carried out by Nield, Manole & Lage (1993) to investigate convection in a horizontal porous layer subjected to thermal and solutal gradients inclined to the vertical. The orientation of the preferred mode and other critical quantities were determined for representative parameter values. The preferred mode can be longitudinal, transverse or oblique, which refer to the orientation of the convective roll axes.

A few experimental results have also been reported concerning double-diffusive convection in porous media with vertical temperature and concentration gradients. Griffiths (1981) used a Hele-Shaw cell and a sand tank model to study the double-diffusive convection in a horizontal porous layer. The presence of a diffusive interface in the cell was used to explain the geothermal system in the Wairakei geothermal fields of New Zealand. Imhoff & Green (1988) used a sand-tank and the salt–sugar system to determine if double-diffusive groundwater fingers can form in a saturated porous medium. Their measurements indicate that double-diffusive groundwater fingers can transport solutes at rates of as much as two orders of magnitude larger than those associated with molecular diffusion in motionless groundwater. Murray & Chen (1989) performed experiments to study double-diffusive convection in a fluid saturated porous medium contained in a box heated from below. The temperature measurements in the longitudinal direction indicated a three-dimensional convection pattern when the porous medium was saturated with a stabilizing salinity gradient, whereas two-dimensional rolls were observed for single-component convection in the same apparatus. They also observed a hysteresis loop in the heat flux curve upon reducing the temperature difference from supercritical to subcritical values, owing to the existence of subcritical regimes.

Studies on double-diffusive convection in tilted porous cavities include that of Mamou, Vasseur & Bilgen (1998) and Karimi-Fard, Charrier-Mojtabi & Mojtabi (1999). The critical stability of the inclined system, including the horizontal position, was investigated (Mamou *et al.* 1998) in terms of the inclination angle by a linear stability analysis based on Galerkin and finite-element methods for opposing but equal thermal and solutal gradients. Their results indicate the occurrence of multiple solutions in the supercritical regime for a given range of governing parameters. Karimi-Fard *et al.* (1999), using the linear stability analysis, studied the onset of double-diffusive convection in a tilted rectangular cavity, filled with a porous medium and saturated by a binary fluid. The critical Rayleigh number for the onset of stationary and oscillatory convection was determined as a function of porosity and Lewis number for different tilt angles, including the horizontal configuration. To confirm the results obtained with the linear stability analysis they also carried out numerical simulations using the finite-volume method. The numerical simulations show multiple subcritical solutions.

The double diffusive convection in a horizontal porous enclosure, subject to vertical gradients of temperature and concentration, was analysed by Mamou &

Vasseur (1999). Analytical solutions were obtained using both linear and non-linear perturbation theories and the parallel flow approximation based on the Darcy model for different boundary conditions. Four different regimes were found to exist and their domain of existence was identified. The results were verified numerically by using a finite-element method. Their numerical results show the existence of multiple solutions for the case of opposing flows in the overstable regime.

All of these theoretical and numerical studies are limited by the two-dimensional flow assumption and nothing can be inferred about the three-dimensional flow patterns. To the best of my knowledge, three-dimensional numerical studies of double-diffusive convection in porous cavities with vertical gradients of temperature and concentration have not been reported prior to the present work. Studies on horizontal porous enclosures saturated with a single fluid and heated from below (Straus & Schubert 1979; Kimura, Schubert & Straus 1986) indicate that the flow is three-dimensional. A similar behaviour may be expected when the porous medium is saturated by a binary fluid with vertical gradients of temperature and concentration. In fact, the rather limited temperature profile measurements reported in the experimental study of Murray & Chen (1989) on double-diffusive convection in a rectangular enclosure, with vertical gradients of temperature and concentration, point out the formation of a three-dimensional flow structure. In the present study, the existence of multiple three-dimensional double-diffusive flow patterns in a horizontal rectangular porous cavity with opposing gradients of temperature and concentration in the fingering regime, where the solute gradient is destabilizing against a stabilizing temperature gradient, is investigated. The main concern here is about the buoyancy-driven convection in the mushy layer formed when a binary alloy is cooled from below as a result of rejection of the lighter component of the mixture upon solidification. The effect of the thermal Rayleigh number, the buoyancy ratio and the Lewis number on the domain of existence of multiple flow patterns are investigated numerically. For the case of a stabilizing solute gradient destabilized by a temperature gradient, the flow transitions and the range of existence of the flow patterns will be different and requires a separate study.

2. Mathematical formulation

The physical model considered in the present study is a horizontal rectangular porous cavity with a square cross-section, having aspect ratios $A_x = L_x/H = 2$, $A_y = L_y/H = 2$ (figure 1) and saturated with a binary fluid. The system is cooled from below where the bottom wall is at a uniform temperature T_2, while the top wall is at a uniform but higher temperature T_1. The resulting stable density gradient is destabilized by a vertical concentration gradient by applying a uniform concentration C_1 of the lighter component of the binary fluid at the bottom wall, while the top wall is maintained at a lower concentration C_2. Zero heat and mass fluxes are imposed on the vertical sidewalls. The binary fluid is assumed to be Newtonian, incompressible and to satisfy the Boussinesq approximation. The porous medium is supposed to be isotropic, homogenous and in thermodynamic equilibrium with the fluid. The Dufour effect is negligible for liquids (Taslim & Narusawa 1986) and the Soret effect decreases at high Lewis numbers and at low permeabilities in a porous medium (Taslim & Narusawa 1986; Rudraiah & Malashetty 1986). In this study, the Soret and Dufour effects are assumed to be negligible. The fluid density is assumed to be constant, except in the driving term of the Navier–Stokes equations, where it

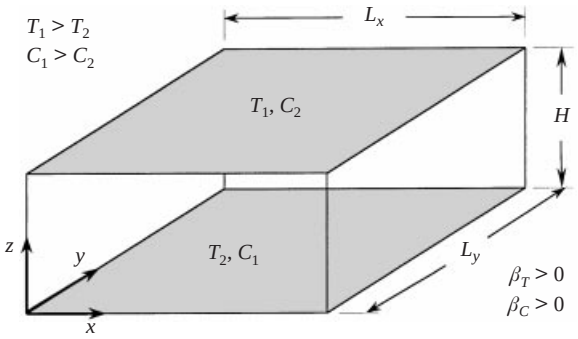

FIGURE 1. Physical model and the coordinate system.

varies linearly with the local temperature and solute mass fraction as

$$\rho = \rho_2[1 - \beta_T(T - T_2) - \beta_C(C - C_2)], \tag{1}$$

where

$$\beta_T = -\frac{1}{\rho_2}\left[\frac{\partial \rho}{\partial T}\right]_C, \quad \beta_C = -\frac{1}{\rho_2}\left[\frac{\partial \rho}{\partial C}\right]_T, \tag{2}$$

with $\beta_T > 0$ and $\beta_C > 0$. The thermophysical properties of the fluid are taken as constant and they are estimated at a reference temperature T_2 and solute mass fraction C_2. Using the following dimensionless variables: $X = x/H$, $Y = y/H$, $Z = z/H$, $\boldsymbol{V} = \boldsymbol{v}H/v$, $P = pH^2/\rho v^2$, $\Theta = (T - T_2)/(T_1 - T_2)$, $\Phi = (C - C_2)/(C_1 - C_2)$, $t = t^*/(H^2/v)$, where v is the kinematic viscosity of the fluid, $\boldsymbol{v}$ is the volume averaged velocity vector, p is the pressure and t^* is time, the equations governing the conservation of mass, momentum, energy and species concentration in non-dimensional form, which include the Forchheimer and Brinkman modifications can be written as,

$$\nabla \cdot \boldsymbol{V} = 0, \tag{3}$$

$$\frac{1}{\varepsilon}\frac{\partial \boldsymbol{V}}{\partial t} + \frac{1}{\varepsilon^2}(\boldsymbol{V}\cdot\nabla)\boldsymbol{V} = -\nabla P + \Lambda\nabla^2\boldsymbol{V} + \frac{Ra_T}{Pr}(\Theta + N\Phi)\boldsymbol{k} - \frac{1}{Da}\boldsymbol{V} - \frac{1.75}{\sqrt{150}}\frac{|\boldsymbol{V}|}{\sqrt{Da}}\frac{\boldsymbol{V}}{\varepsilon^{3/2}}, \tag{4}$$

$$\sigma\frac{\partial \Theta}{\partial t} + \boldsymbol{V}\cdot\nabla\Theta = \frac{1}{Pr}\lambda\nabla^2\Theta, \tag{5}$$

$$\varepsilon\frac{\partial \Phi}{\partial t} + \boldsymbol{V}\cdot\nabla\Phi = \frac{1}{Le\,Pr}\nabla^2\Phi, \tag{6}$$

where $Le = \alpha/D$ is the Lewis number $Ra_T = (g\beta_T\Delta T H^3)/v\alpha$ the thermal Rayleigh number, $N = Ra_C/(Ra_T Le)$ the buoyancy ratio, $Ra_C = (g\beta_C\Delta C H^3)/vD$ the solutal Rayleigh number, $\Delta T = T_1 - T_2$, $\Delta C = C_1 - C_2$, $Da = K/H^2$ the Darcy number, $Pr = v/\alpha$ the Prandtl number and $\alpha = k/\rho_2 C_p$ is the effective thermal diffusivity. The parameters K and ε are the permeability and porosity of the porous medium, g, $\boldsymbol{k}$, C_p, D and k, refer to the acceleration due to gravity, unit vector in the vertical direction, specific heat, molecular diffusivity of the fluid and effective thermal conductivity, respectively. The Brinkman term is included in the momentum equation (4) to account for the viscous stresses adjacent to the bounding walls. The parameter $\Lambda = \mu'/\mu$ is the ratio of the effective viscosity in the Brinkman term to fluid viscosity. The variation in Λ is not fully understood and most of the works on non-Darcy formulation consider $\Lambda = 1$. In the momentum equation, the last term is the Forchheimer term

and represents the nonlinear drag effect due to the solid matrix, where Ergun's (1952) correlation is used with the total velocity vector $|\boldsymbol{V}| = (U^2 + V^2 + W^2)^{0.5}$. Lauriat & Prasad (1989) point out that at least for the Ergun model, the Forchheimer term becomes important long before the contribution of the Brinkman term is of any significance for natural convection flows and that any consideration of non-Darcy effects requires both the Forchheimer and Brinkman terms to be considered simultaneously. Even though the contribution of the advection terms is small for a porous medium they are included in the model to handle all possible situations. Also, for smooth development of the boundary layer near the walls inclusion of advection terms is necessary (Vafai & Kim 1995). $\lambda = k_m/k_f$ is the ratio of thermal conductivities of the porous medium and the fluid and $\sigma = [\varepsilon(\rho c_p)_f + (1-\varepsilon)(\rho c_p)_s]/(\rho c_p)_f = (\rho c_p)_m/(\rho c_p)_f$ is the heat capacity ratio.

The boundary conditions used are:

$$U = V = W = \frac{\partial \Theta}{\partial X} = \frac{\partial \Phi}{\partial X} = 0 \quad \text{for } X = 0, A_x, \tag{7}$$

$$U = V = W = \frac{\partial \Theta}{\partial Y} = \frac{\partial \Phi}{\partial Y} = 0 \quad \text{for } Y = 0, A_y, \tag{8}$$

$$U = V = W = 0, \quad \Theta = 0, \quad \Phi = 1 \quad \text{for } Z = 0, \tag{9}$$

$$U = V = W = 0, \quad \Theta = 1, \quad \Phi = 0 \quad \text{for } Z = 1, \tag{10}$$

where U, V and W are the x, y and z components of the velocity vector, respectively. The average heat and mass fluxes at the top wall are given in the non-dimensional terms by Nusselt and Sherwood numbers as

$$Nu_{ave} = \int_0^{A_y} \int_0^{A_x} \left[\frac{\partial \Theta}{\partial Z}\right]_{Z=1} \mathrm{d}X\,\mathrm{d}Y, \quad Sh_{ave} = \int_0^{A_y} \int_0^{A_x} \left[\frac{\partial \Phi}{\partial Z}\right]_{Z=1} \mathrm{d}X\,\mathrm{d}Y. \tag{11}$$

3. Numerical method

The governing equations (3)–(6) are solved numerically using the control volume formulation with staggered, non-uniform grids. Since the details of the present numerical procedure are discussed elsewhere (Sezai & Mohamad 1999) only the main steps are presented here. The QUICK scheme is used in approximating the advection terms together with ULTRA-SHARP as the flux limiter (Leonard & Mokhtari 1990). The SIMPLEC algorithm (Van Doormaal & Raithby 1984) is used to couple momentum and continuity equations. The momentum equations are solved by using the strongly implicit procedure (SIP) of Stone (1968). The pressure correction equation is solved iteratively by applying the conjugate gradient (CG) method (Hackbush 1994) and the energy and species concentration equations are solved iteratively by the Bi-CGSTAB method (Van der Vorst 1992). SSOR preconditioning (Hackbush 1994) is used for accelerating the convergence rates of both CG and Bi-CGSTAB methods.

To avoid the excessively high computer times inherent in the solution of three-dimensional natural convection problems, a full approximation storage (FAS) full multigrid (FMG) method (Hortmann, Peric & Scheuerer 1990) is used to solve the problem, which removes a wider spectrum of wavelengths more efficiently than single-grid methods. The equations are solved by a four-level fixed V-cycle procedure (Hortmann *et al.* 1990; Shyy & Sun 1993). In this method, the solution obtained on a coarse grid is transferred to the next finer grid and the process is repeated until the finest grid level is reached. Then, the residuals are transferred to the next coarser grid,

where the fine-grid solution is corrected. The process is repeated down to the coarsest grid level. The whole process is repeated until a converged solution is obtained on the finest grid level. $96 \times 96 \times 48$ control volumes are used on the finest level for all cases except for the time-dependent solutions where $48 \times 48 \times 24$ control volumes are used. The time stepping has been realized with the second-order, fully implicit, backward Euler scheme.

The computer code has been validated for various cases and the results published elsewhere (Sezai & Mohamad 1999, 2000).

4. Results and discussion

The numerical model is used to investigate double-diffusive fingering convection in a horizontal porous enclosure having aspect ratios $A_x = A_y = 2$ and subjected to vertical but opposing gradients of temperature and concentration. Since concentration refers to the lighter component of the binary mixture ($\beta_C > 0$) then, with higher concentration at the bottom, Ra_C is positive. Since β_T is positive, then Ra_T is also positive, resulting in a positive N value for the given boundary conditions. Thus, the temperature gradient is stabilizing, whereas the concentration gradient is destabilizing.

Simulations were carried out starting with the diffusion solution and increasing either N, Ra^* or Le to a point beyond which unsteady flow starts. The effect of the buoyancy ratio is investigated by varying N between 0.5 and 4.5 with Ra^* held constant at 10 and Le at 10. The porous thermal Rayleigh number $Ra^* = Ra_T Da$ is varied between 10 and 100, while N is fixed at 0.5 and Le at 10. Furthermore, the effect of the Lewis number is investigated by varying Le between 10 and 240 for $Ra^* = 5$ and $N = 0.5$. The Prandtl number of the fluid is fixed at $Pr = 10$. The thermal properties of the solid porous matrix and the fluid have been taken to be identical so that $\lambda = 1$ and $\sigma = 1$. The porosity of the medium is assumed to be uniform throughout the domain and to remain constant with time at $\varepsilon = 0.6$. The remaining properties of the porous medium are set as $\Lambda = 1$ and $Da = 10^{-5}$. Both time-dependent and steady solutions were obtained in the present investigation. To speed up convergence, steady solutions on a solution branch, that have the same flow structure, have been obtained by switching off the time derivative terms in equations (4)–(6) and the resulting steady-state equations have been solved by using the results obtained from the previous run as input for the next run. However, for transitions from one solution branch to the other, or for cases where convergence problems were met, the full time-dependent equations were used. The transitions can involve a change in the steady flow patterns, a change from steady to unsteady flow patterns or a change from unsteady to steady flow patterns.

4.1. *Symmetry properties*

The nonlinear differential equations (3)–(6) together with the boundary conditions (7)–(10) admit solutions with some symmetries. Before presenting the results it is worth summarizing the symmetry properties of the structures obtained and classifying them in terms of symmetry groups.

4.1.1. *Plane symmetries*

(*i*) Plane symmetry s_y with respect to $Y = 1$:

$$s_y \boldsymbol{Q} = \boldsymbol{Q}, \tag{12}$$

where $\boldsymbol{Q}$ represents the solution (U, V, W, Θ, Φ) and s_y is the mapping which produces

the mirror image of the flow field, together with the temperature and concentration fields about the $Y = 1$ plane with by definition

$$s_y : (X, Y, Z, t) \to (X, 2 - Y, Z, t), \quad (U, V, W, \Theta, \Phi) \to (U, -V, W, \Theta, \Phi).$$

If $\boldsymbol{Q}$ is a solution of the problem, then $s_y \boldsymbol{Q}$ is also a solution.

(*ii*) Plane symmetry s_x with respect to $X = 1$:

$$s_x \boldsymbol{Q} = \boldsymbol{Q}, \tag{13}$$

with, by definition,

$$s_x : (X, Y, Z, t) \to (2 - X, Y, Z, t), \quad (U, V, W, \Theta, \Phi) \to (-U, V, W, \Theta, \Phi).$$

In cases where the solution is plane symmetric, the velocity component perpendicular to the symmetry plane is zero on that plane. For example, if the solution has plane symmetry s_x with respect to the $X = 1$ plane, then $U = 0$ on plane $X = 1$.

(*iii*) Plane symmetry s_d with respect to the diagonal plane $X = Y$:

$$s_d \boldsymbol{Q} = \boldsymbol{Q}, \tag{14}$$

where s_d is the mapping which produces a mirror image of the T, C and the flow fields about the $X = Y$ plane with by definition

$$s_d : (X, Y, Z, t) \to (Y, X, Z, t), \quad (U, V, W, \Theta, \Phi) \to (V, U, W, \Theta, \Phi).$$

(*iv*) Plane symmetry $s_{d'}$ with respect to the diagonal plane $X = -Y$:

$$s_{d'} \boldsymbol{Q} = \boldsymbol{Q} \tag{15}$$

where $s_{d'}$ is the mapping which produces a mirror image of the T, C and the flow fields about the $X = -Y$ plane with, by definition,

$$s_{d'} : (X, Y, Z, t) \to (2 - Y, 2 - X, Z, t), \quad (U, V, W, \Theta, \Phi) \to (-V, -U, W, \Theta, \Phi).$$

4.1.2. *Rotational symmetries*

(*i*) Rotational symmetry r^2 with respect to a vertical axis at $X = 1$, $Y = 1$:

$$r^2 \boldsymbol{Q} = \boldsymbol{Q}, \tag{16}$$

where r is the mapping which consists of a rotation of 90° with respect to the vertical axis (parallel to the z-axis) at $X = 1$, $Y = 1$. Here, r^2 is shorthand for rr which means applying r twice and is equivalent to a rotation of 180°. That is,

$$r^2 : (X, Y, Z, t) \to (2 - X, 2 - Y, Z, t), \quad (U, V, W, \Theta, \Phi) \to (-U, -V, W, \Theta, \Phi).$$

(*ii*) Rotational symmetry r_y^2 with respect to the horizontal axis at $X = 1$, $Z = 0.5$:

$$r_y^2 \boldsymbol{Q} = \boldsymbol{Q}, \tag{17}$$

where r_y^2 is the mapping which consists of a rotation of 180° with respect to the horizontal axis at $X = 1$, $Z = 0.5$, with, by definition,

$$r_y^2 : (X, Y, Z, t) \to (2 - X, Y, 1 - Z, t), \quad (U, V, W, \Theta, \Phi) \to (-U, V, -W, 1 - \Theta, 1 - \Phi).$$

(*iii*) Translational symmetry in space, τ:

$$\tau \boldsymbol{Q} = \boldsymbol{Q}, \tag{18}$$

with

$$\tau : (X, Y, Z, t) \to (X + \lambda_x, Y + \lambda_y, Z + \lambda_z, t), \quad (U, V, W, \Theta, \Phi) \to (U, V, W, \Theta, \Phi),$$

which moves the pattern by distances λ_x, λ_y and λ_z in the x-, y- and z-directions, respectively. A single symmetry operation such as r^2 generates the symmetry group $\{e, r^2\}$, where e is the identity. This group is called Z_2. Similarly, single plane reflections generate the symmetry groups such as $\{e, s_x\}$, $\{e, s_y\}$, $\{e, s_d\}$ and $\{e, s_{d'}\}$, which are all isomorphic to Z_2. We shall use the name Z_2 to describe the structure of all these groups. A rectangle has three symmetries: 180° rotation r^2, as well as plane symmetries s_x and s_y. So, the symmetry group of a rectangle is

$$\{e, s_x, s_y, r^2\}, \tag{19}$$

and is called D_2. Applying the symmetry operations s_x and s_y consecutively is equivalent to 180° rotation about a vertical axis. That is, $r^2 = s_x s_y = s_y s_x$. The group D_2 has three subgroups $\{e, s_x\}$, $\{e, s_y\}$ and $\{e, r^2\}$. Any two of these three Z_2 subgroups can be combined to form D_2, and is written as $D_2 = Z_2 \times Z_2$. In general, a group G with elements g_i contains a subgroup H with elements h_i if all products $h_i h_j$ are elements of both H and G (Armstrong 1988).

A square has four more symmetries: s_d and $s_{d'}$ corresponding to reflections about the two diagonals, and r and r^3 corresponding to 90° and 270° rotations about the vertical centreline. So the symmetry group of a square is

$$\{e, s_x, s_y, s_d, s_{d'}, r, r^2, r^3\}, \tag{20}$$

and is called D_4. The cyclic group Z_4 given by $\{e, r, r^2, r^3\}$ is a subgroup of D_4.

In general, Z_n can be considered to be the rotational symmetry group of an n-gon, without reflections and has n-elements. On the other hand, the dihedral group D_n contains the rotational symmetries of Z_n combined with a reflection and has $2n$ elements. Similarly, the symmetry group of a rectangular prism is $D_{2h} = D_2 \times Z_2$ and has 8 elements. The symmetry group of a square prism is $D_{4h} = D_4 \times Z_2$ and has 16 elements. The symbols Z_2, D_2, D_4, D_{4h} etc. will also be used for any groups that are isomorphic to these groups, regardless of what physical operation the elements of the group represent.

The initial motionless diffusion state has D_4 symmetry owing to the square horizontal cross-section of the domain, but it is also invariant by any horizontal translation, since both temperature and concentration are independent of the x- and y-directions, but depend only on z. The patterns bifurcating from this solution will have symmetries that form a subgroup of D_{4h}, which is the product of D_4 and this group of translations. The symmetries can be broken through bifurcations. There is a close relationship between the change of symmetry and the nature of the bifurcation. A bifurcation from one structure to the other is a pitchfork type if one of the symmetries is broken and it is transcritical if the symmetries are preserved after bifurcation. In the present study, a total of 36 symmetric flow structures have been obtained at steady state.

Figure 2 illustrates the symmetric flow structures and three of the non-symmetric structures found. In the figure, the local distributions of the Sherwood number on the top plate, the projection of the flow lines on a horizontal plane at $Z = 0.9$, the projection of flow lines on the mid (x, z)- and the mid (y, z)-planes are displayed. The projections of flow lines on a particular plane are obtained from the in-plane components of the velocity vectors on that plane. For example, the projection of flow lines on an (x, y)-plane is obtained by using the U and V components of velocities on that plane. The locations of maximum values of the local Sherwood number indicate impingement regions caused by the flow coming from the bottom whereas minimum values indicate stagnant regions of boundary-layer development for the fluid leaving

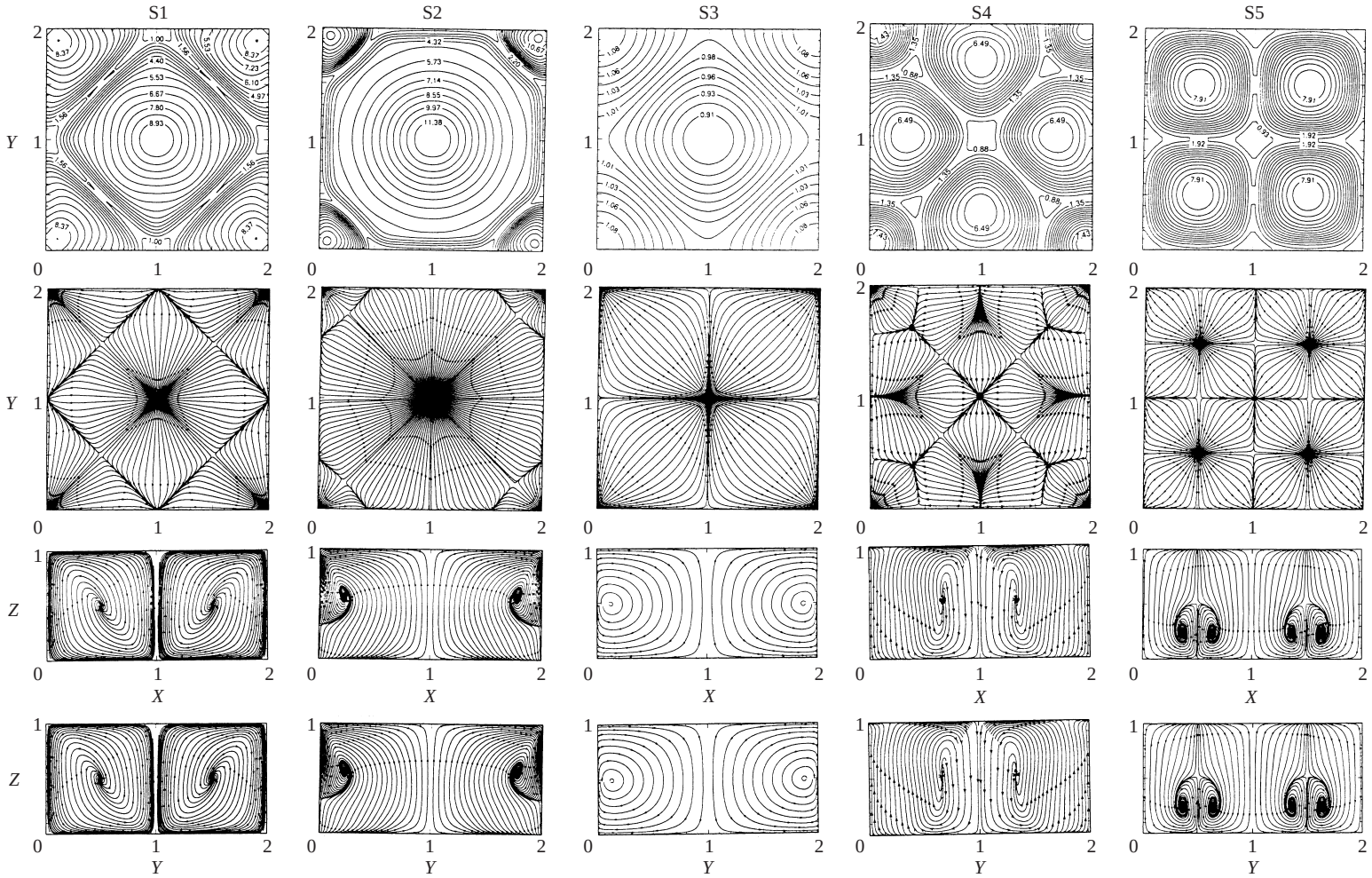

FIGURE 2. For caption see page 327.

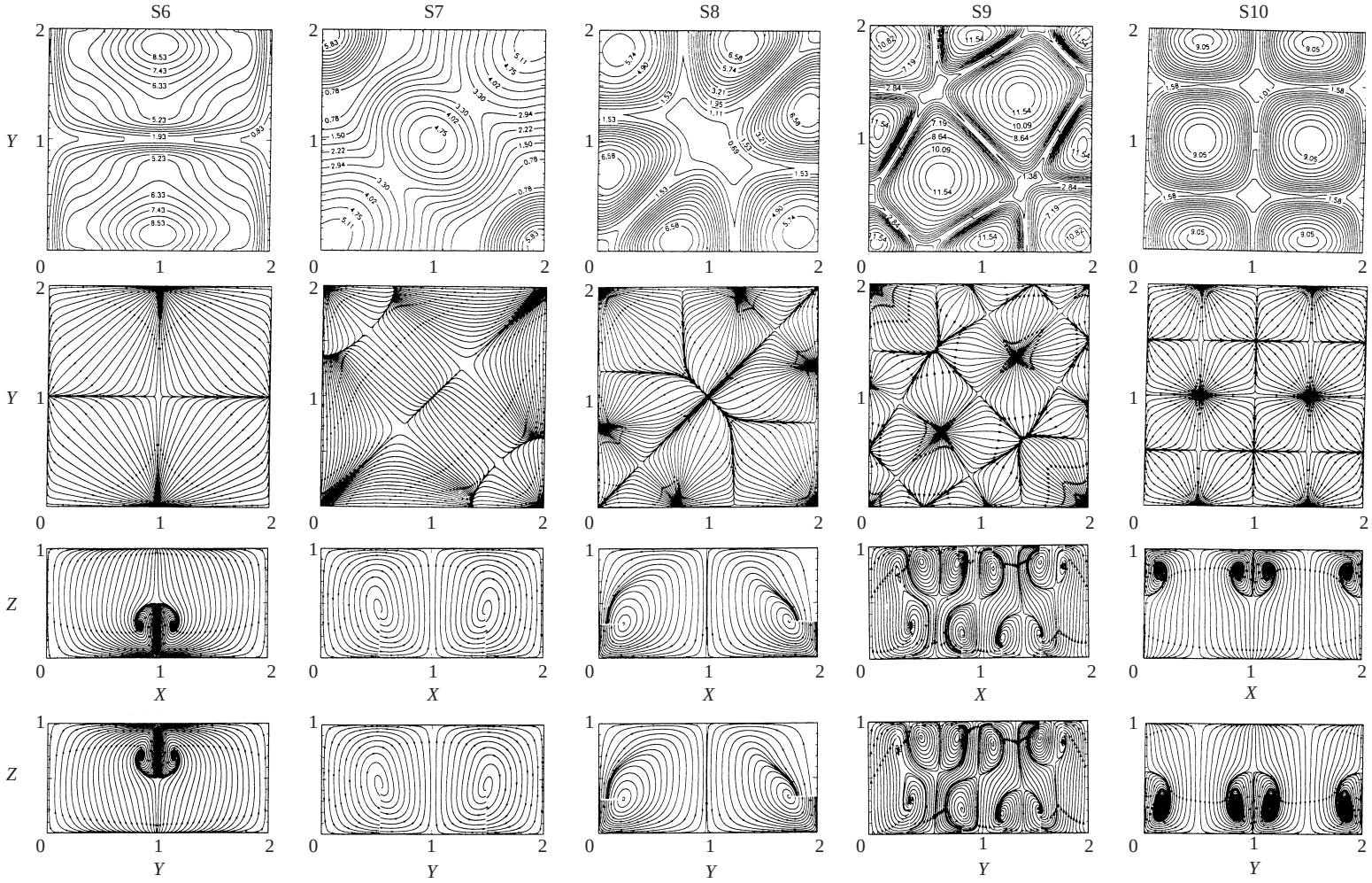

FIGURE 2. For caption see page 327.

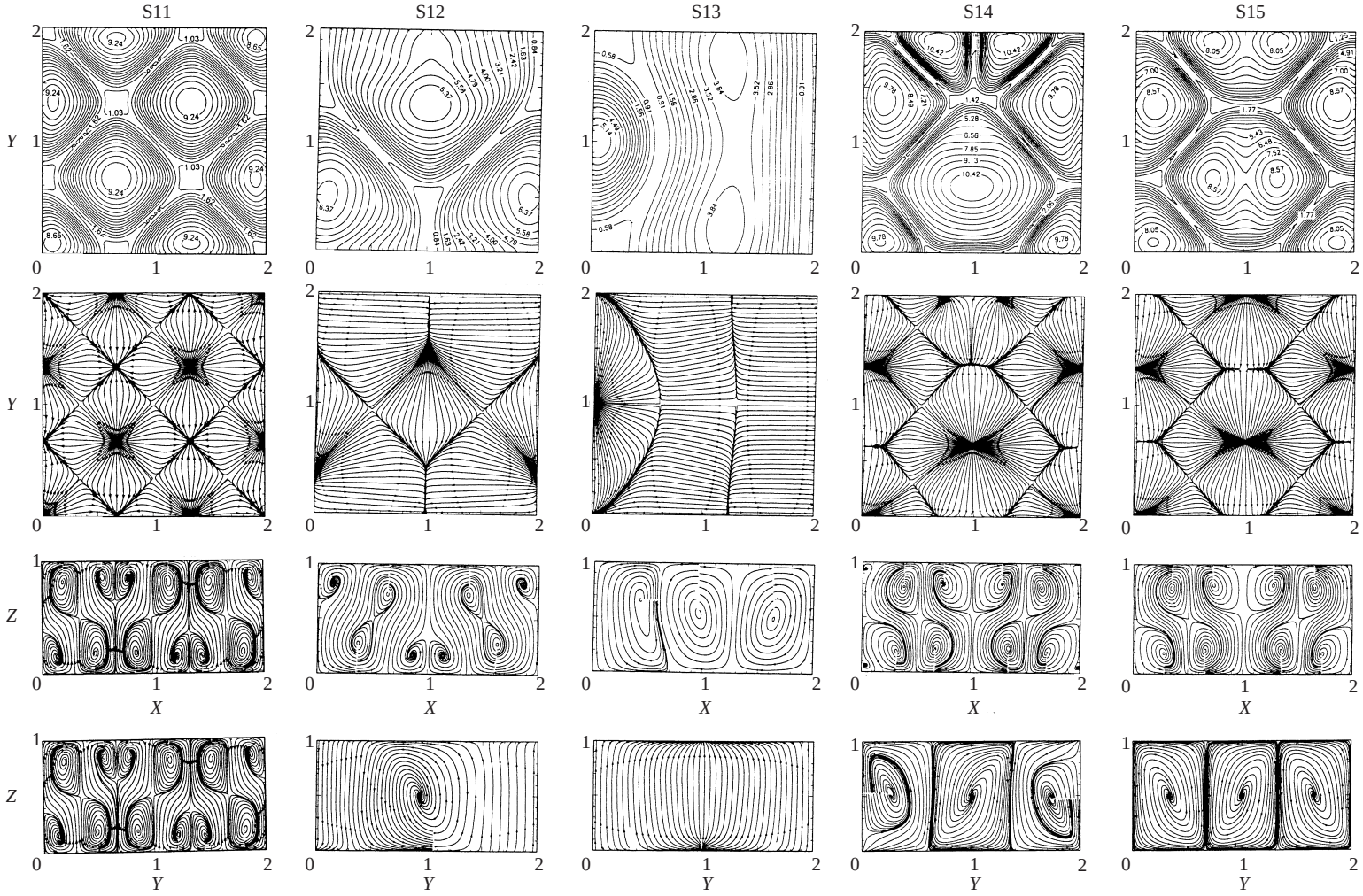

FIGURE 2. For caption see page 327.

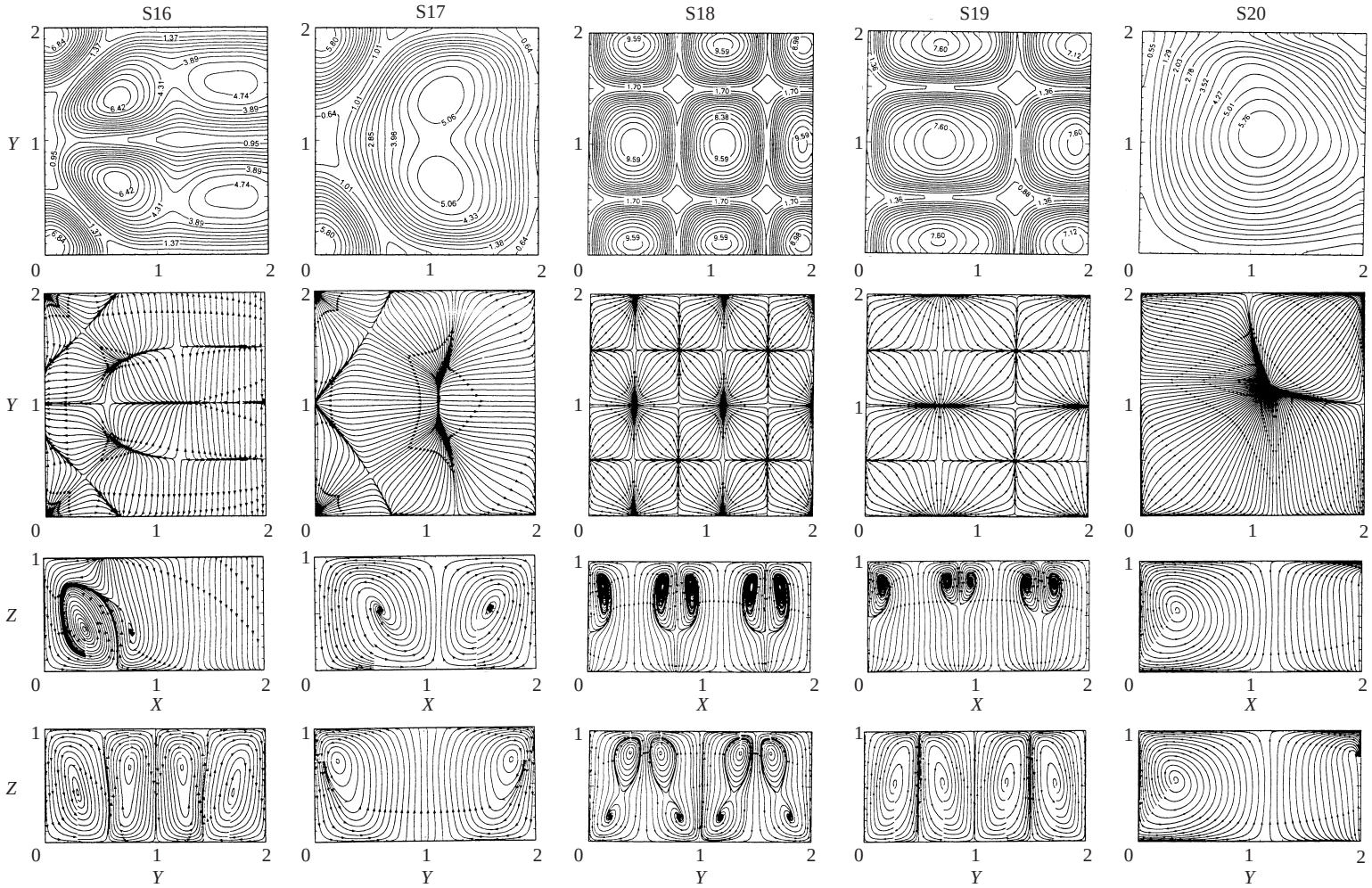

FIGURE 2. For caption see page 327.

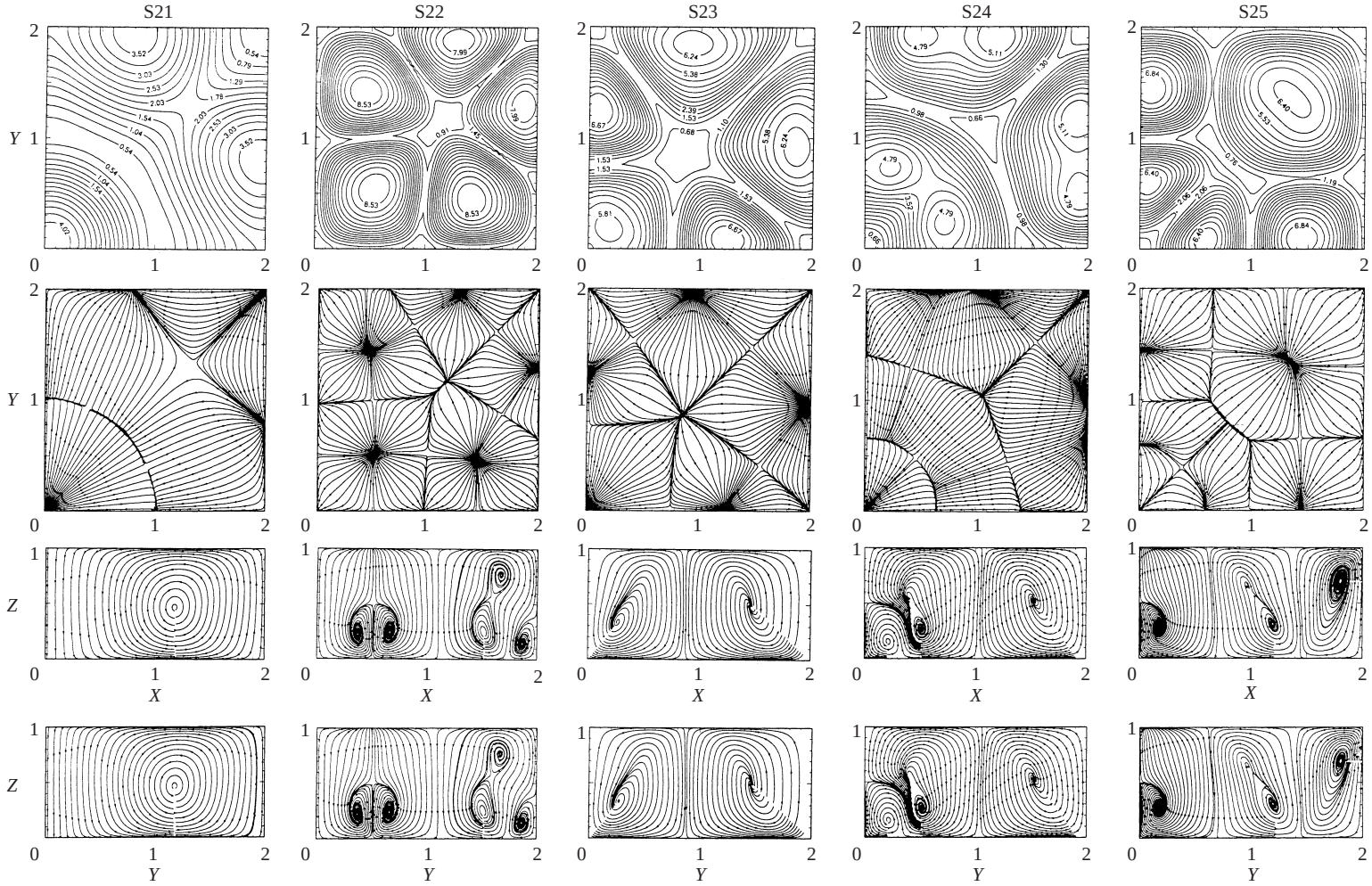

FIGURE 2. For caption see page 327.

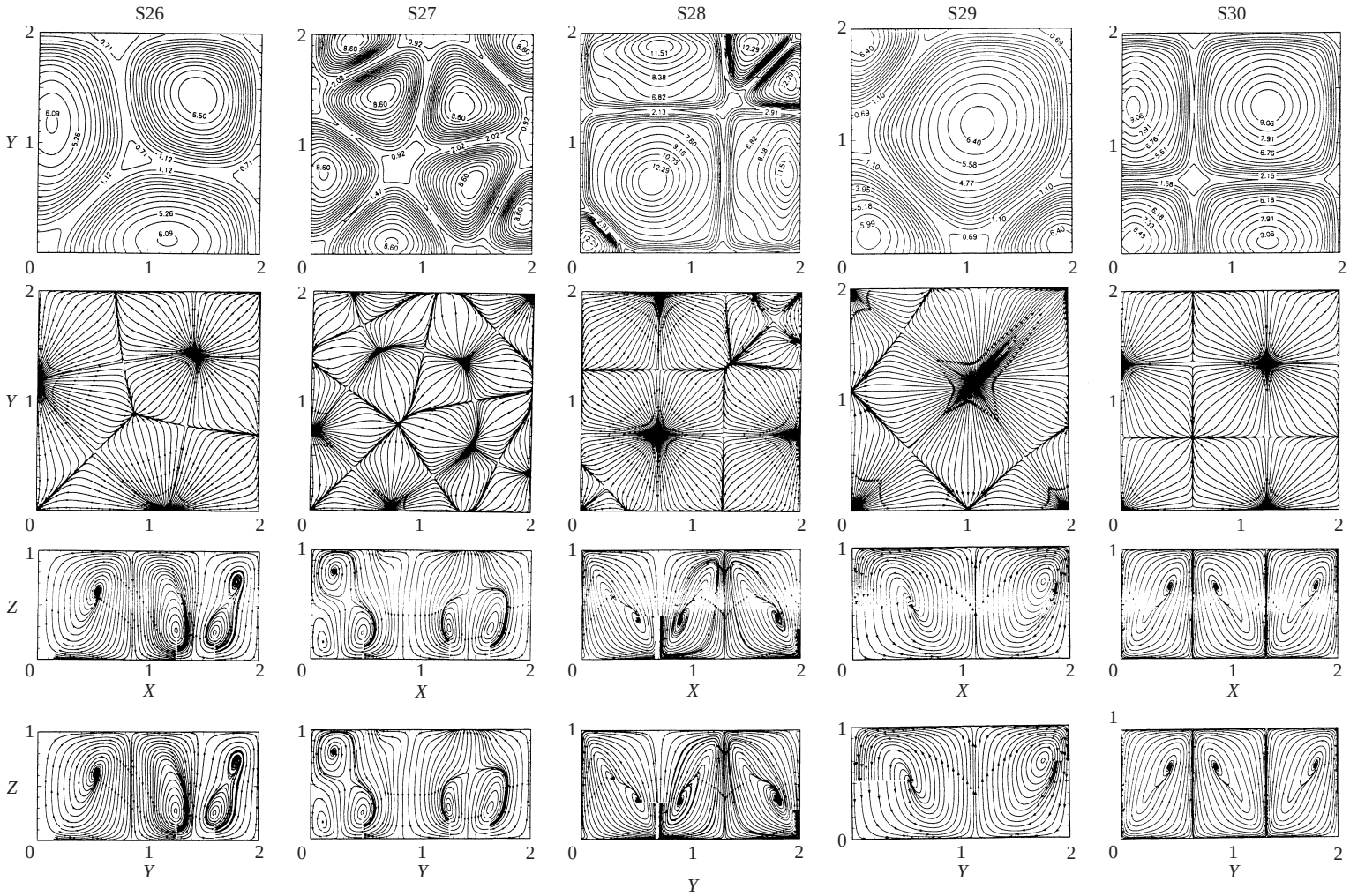

FIGURE 2. For caption see page 327.

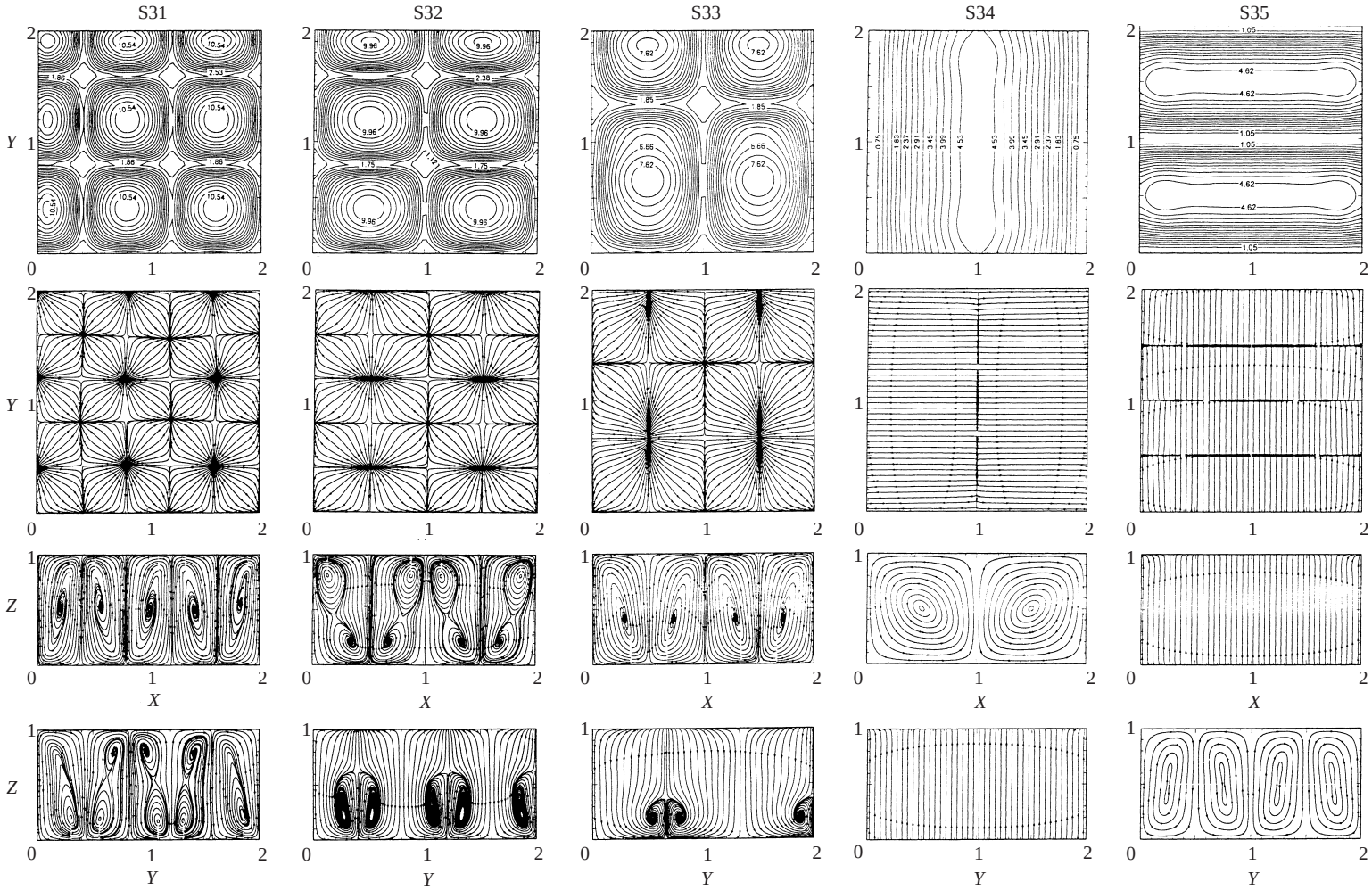

FIGURE 2. For caption see page 327.

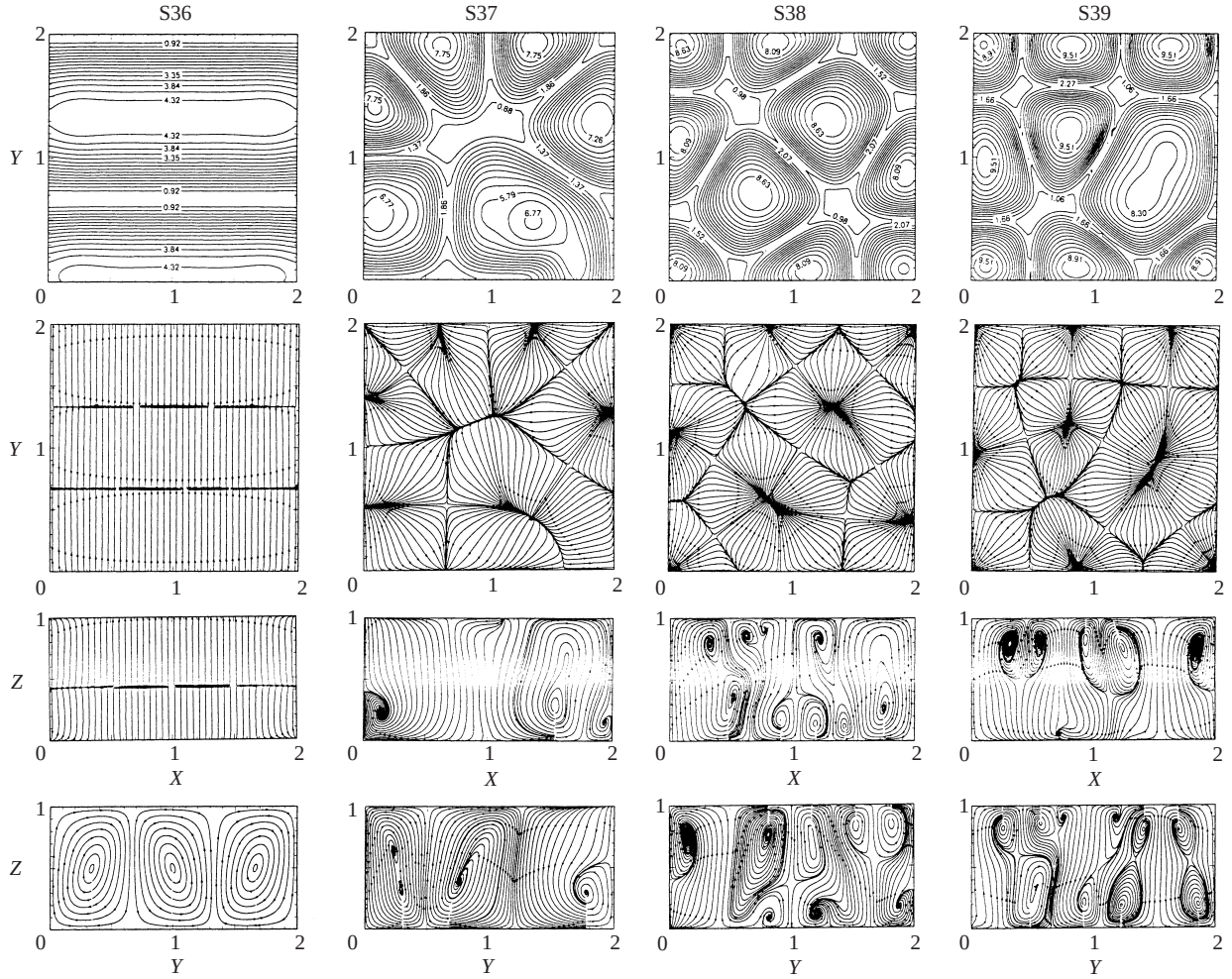

FIGURE 2. Convection structures developed in the cavity. Top row: Sh distribution at top plate; second row: projection of flow lines on the horizontal plane at $Z = 0.9$; third row: projection of flow lines on the mid (x, z)-plane; fourth row: projection of flow lines on the mid (y, z)-plane.

Pattern	Symmetry group
S1–S4	D_4
S5	D_{4h}
S6–S9	D_2
S10–S11	D_{2h}
S12–S31	Z_2
S32–S33	$Z_2 \times Z_2 = D_2$
S34	$Z_2 \times O_2$
S35–S36	$D_2 \times O_2$
S37–S39	NS

TABLE 1. Symmetry groups.

the top plate. The corresponding Nusselt number distributions are quite similar to the local Sherwood number distributions and for this reason they are not included in the figure.

The symmetry group of each flow pattern is given in table 1. Structures S1–S4 have D_4 symmetry. Structure S5 also has D_4 symmetry, but is in addition invariant under the translational symmetry $\tau_{xy} : (X, Y, Z, t) \rightarrow (X + \frac{1}{2}A_x, Y + \frac{1}{2}A_x, Z, t)$, which moves the pattern by $\frac{1}{2}A_x$ in the x- and y-directions taking one upward plume to the other. Combining the rotations and reflections of D_4 with the translation τ (which generates the group Z_2) results in the group D_{4h}.

Structures S6–S9 belong to the D_2 group having symmetries $\{e, s_d, s_{d'}, r\}$. Structure S10 also has D_2 symmetry, but in addition it is invariant under the translational symmetry $\tau_x : (X, Y, Z, t) \rightarrow (X + \frac{1}{2}A_x, Y, Z, t)$, that moves the pattern by $\frac{1}{2}A_x$ in the x-direction and thus belongs to group D_{2h}. The flow pattern S11 has D_2 symmetry $\{e, s_d, s_{d'}, r\}$, but it is also invariant after a 180° rotation r_y^2 about a horizontal axis passing through the centre and thus belongs to group $D_2 \times Z_2 = D_{2h}$. Structures S12–S31 belong to the Z_2 group. Of these structures, S12–S19 have plane symmetries $\{e, s_x\}$ or $\{e, s_y\}$. The two are equivalent since one is a 90° rotated version of the other. The other structures in the Z_2 group (S20–S31) have single diagonal symmetries $\{e, s_d\}$ or $\{e, s_{d'}\}$. The flow structures S32 and S33 also have Z_2 symmetry, but in addition they also have translation symmetry $\tau_x : (X, Y, Z, t) \rightarrow (X + \frac{1}{2}A_x, Y, Z, t)$, which moves the pattern by $\frac{1}{2}A_x$ in the x-direction and thus they belong to symmetry group $Z_2 \times Z_2 = D_2$.

The pattern consisting of two rolls in S34 together with its temperature and concentration profiles is approximately two-dimensional disregarding the endwall effects near $Y = 0$ and $Y = 2$. Then, structure S34 is unchanged after reflecting in the y-direction and after translating by any amount in the same direction yielding the symmetry group $O(2)$ of a circle under rotations and reflections. That is, in the O_2 group the pattern is unchanged under the reflection $s_y : (X, Y, Z, t) \rightarrow (X, 2 - Y, Z, t)$ and translation $\tau_y : (X, Y, Z, t) \rightarrow (X, Y + \lambda_y, Z, t)$. The rolls are also unchanged after reflecting in the x-direction, so the symmetry group S34 is $Z_2 \times O(2)$. Similarly, approximately two-dimensional four rolls in S35 have $O(2)$ symmetry and are also invariant under reflection s_y in the y-direction. In addition, this pattern is invariant under the translation symmetry $\tau_y : (X, Y, Z, t) \rightarrow (X, Y + \frac{1}{2}A_y, Z, t)$, which moves the pattern by $\frac{1}{2}A_y$ in the y-direction, so the symmetry group of the four rolls is $Z(2) \times Z(2) \times O(2) = D_2 \times O(2)$. The three rolls in S36 have $O(2)$ symmetry and the

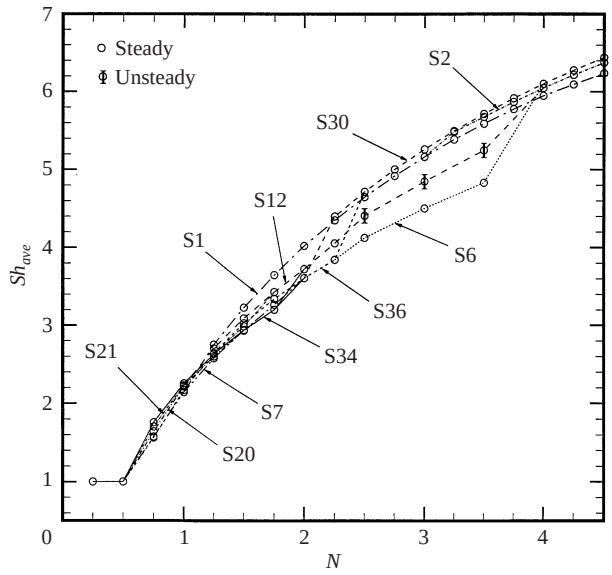

FIGURE 3. Variations of average Sherwood number with buoyancy ratio. $Ra^* = 10$; $Le = 10$.

pattern is also invariant under the translation symmetry which moves the pattern by $\frac{2}{3}A_y$ in the y-direction. In addition, the rolls have rotational symmetry r_x around the horizontal axis at $Y = 1$, $Z = 0.5$, so they belong to group $Z_2 \times Z_2 \times O(2)$. Non-symmetric flow structures have also been obtained of which three are shown in figure 2 named as S37, S38 and S39.

The topologies of all structures, the flow transitions between them and the corresponding mass transfer characteristics are discussed in the following subsections.

4.1.3. *Effect of buoyancy ratio*

Figure 3 depicts the variation of the average Sherwood number with the buoyancy ratio for $Ra^* = 10$. The average Nusselt number changes between 1.0 and 1.3 in the range of buoyancy ratios investigated, indicating a diffusion dominated heat transfer. The transitions from one structure to the other are shown by arrows. Figure 4 shows the transitions between the different flow structures as a function of the buoyancy ratio.

Starting from diffusive temperature and concentration profiles as initial conditions, the buoyancy ratio is increased in steps using the results from the previous run as input for the next run. At low buoyancy ratios, the trivial (diffusive) solution is stable and is the only solution for $N < 0.52$. At $N = 0.52$, the system undergoes a supercritical bifurcation to the two-roll structure S34, where no hysteresis phenomena are observed with decreasing buoyancy ratios. Using the results of the linear stability analysis of Nield (1968) for a horizontal layer of saturated porous medium, the critical value of the buoyancy ratio for the onset of convection can be determined from $N = (Ra^* + 4\pi^2)/(Ra^* Le)$. For $Ra^* = 10$ and $Le = 10$, the critical value of N for a horizontal porous layer is predicted to be 0.495. The value of the critical buoyancy ratio found from the present numerical simulation is slightly above the value pedicted for a horizontal porous layer. Structure S34 has $Z_2 \times O_2$ symmetry and consists of two horizontal rolls, which are almost two-dimensional with three-dimensional effects noticeable near the endwalls. The orientation of the rolls may be along the x- or

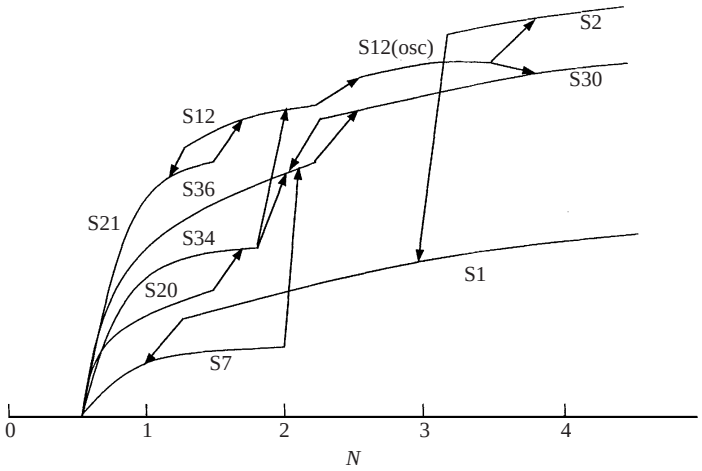

FIGURE 4. Schematic diagram of the flow transitions as a function of buoyancy ratio.

y-direction and both cases are denoted by S34. This is the form of the structure found in the two-dimensional study of Chen & Chen (1993) for an enclosure of aspect ratio 2. The single-roll structure found in the two-dimensional study of Mamou & Vasseur (1999) for enclosures having aspect ratio greater than one, could not be obtained in the present study.

Structure S34 is stable up to $N = 1.7$ and depending on the time step used, it bifurcates to either the three-roll structure S36, having $Z_2 \times Z_2 \times O_2$ symmetry, or to structure S12, where O_2 symmetry is completely lost and only $\{e, s_x\} = Z_2$ symmetry is retained. Upon increasing N further, S36 bifurcates to the upper branch S30, where the plane symmetry s_x is replaced by the diagonal plane symmetry s_d. Structures on this branch produce four-roll cells of which two are of equal size and the other two are different. The rising high-concentration fluids produce four maxima in the Sherwood number distribution at the top plate. Structure S30 is stable at high buoyancy ratios up to 4.5, which is the highest N value investigated. When N is decreased from 2.2 to 2.0 this structure evolves back to S36 forming a hysteresis loop.

The diagonally aligned roll structure S20 is characterized by a rising high-concentration fluid displaced from the centreline and has $\{e, s_d\} = Z_2$ symmetry. This structure is stable up to $N = 1.5$, where it bifurcates to the two-roll structure S34 having $Z_2 \times O_2$ symmetry as N is increased further. At higher buoyancy ratios, S34 may jump to either the three-roll structure S36 or to Z_2 symmetric structure S12 by losing its O_2 symmetry. Structure S12, is three-dimensional with three ascending currents of high concentration fluid; one of them located near the centre and two near the corners (figure 2). These currents impinge at the top plate causing three corresponding maxima in the Sherwood number distribution. Structure S12 bifurcates to a periodic state through a Hopf bifurcation at $N \approx 2.5$, where the plane symmetry is preserved during the oscillations. Figure 5 depicts the time variation of the average Sherwood number and its time mean value at the top plate and the power spectra of its deviation from the time average value when N is increased from 2.0 to 2.5 and using the steady-flow structure S12 as the initial condition.

As N is increased to 3.0, the plane symmetry is broken by small-scale oscillations. The power spectrum of the deviation of the average Sherwood number from its time average value is shown in figure 6 for $N = 3.0$. The power spectrum reveals two

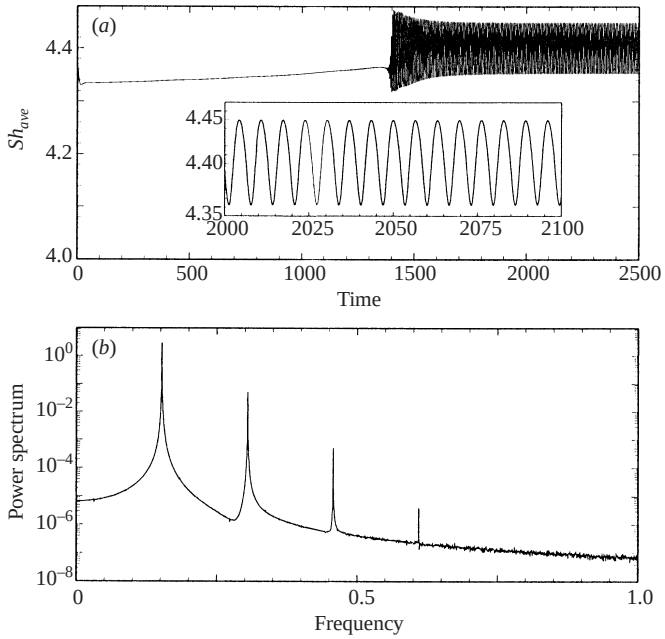

FIGURE 5. (*a*) Time variation of the average Sherwood number at the top plate and (*b*) the power spectra of its deviation from time mean value for the transition of structure S12 from steady to unsteady flow.

independent fundamental frequencies. In the classification scheme of Gollub & Benson (1980), a quasi-periodic oscillatory state with two fundamental incommensurate frequencies is denoted as quasi-periodic and if the frequencies are in a rational ratio then the state is periodic. With this classification, the flow in figure 6 is quasi-periodic. Increasing the buoyancy ratio to 3.5, with the solution at $N = 3.0$ as initial conditions, results in the loss of quasi-periodicity, as shown by the Sherwood number variations in figure 7. The strong broadband noise in the power spectrum suggests that the flow is in a chaotic regime. However, when N is increased further to 4.0 the flow evolves to the steady, toroidal roll structure S2 which belongs to $\{e, s_x, s_y, s_d, s_{d'}, r, r^2, r^3\} = D_4$ symmetry group, or to the branch of solutions S30 having a diagonal plane $\{e, s_d\} = Z_2$ symmetry. Structure S2 becomes unstable for $N < 3.25$, where it undergoes a transcritical bifurcation to another D_4 group toroidal roll structure S1, preserving all of its symmetries. As N is reduced further, it bifurcates to S7, losing its s_x and s_y symmetries, and retains only the $\{e, s_d, s_{d'}, r^2\} = D_2$ symmetry.

4.1.4. *Effect of porous thermal Rayleigh number*

The variations of the average Sherwood number with porous thermal Rayleigh number is given in figure 8, for $N = 0.5$ and $Le = 10$. A schematic diagram showing the transitions between the flow structures is given in figure 9. Starting with the diffusive solution as initial conditions, where the temperature gradient is positive and the concentration gradient is negative, convection starts at $Ra^* \approx 11$. Using Nield's (1968) criteria, the critical value of porous thermal Rayleigh number for a horizontal porous layer can be found from $Ra^* = 4\pi^2/(NLe - 1)$, which yields a value of 9.870. The critical value found in the present study for the three-dimensional cavity is slightly higher than this value. At low Rayleigh numbers, the trivial diffusive solution is stable and is the only solution for $Ra^* < 11$. At this point, the system

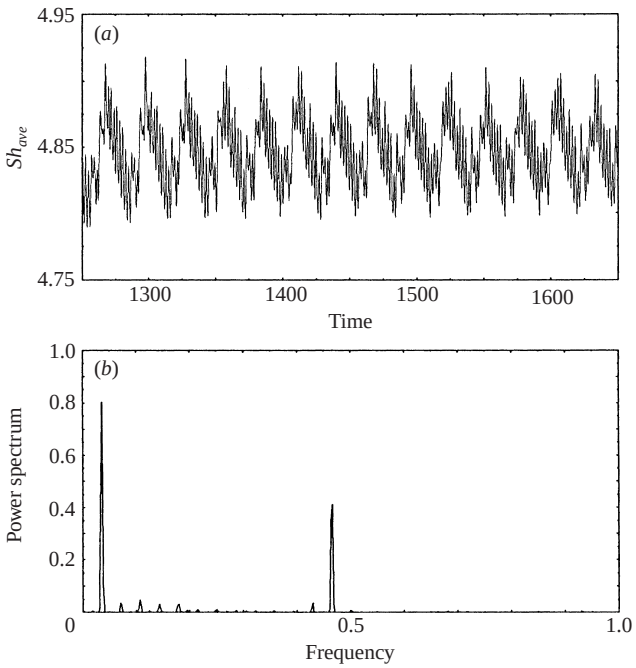

FIGURE 6. (*a*) Time variation of the average Sherwood number and (*b*) the power spectra of its deviation from the time mean value for $N = 3.0$ for structure S12.

undergoes a transcritical bifurcation to structure S3, having D_4 symmetry. For this solution, the motion sets in, taking the form of a toroidal roll in which the fluid rises from the centre. A toroidal roll may also form, where the descending fluid is at the centre, depending on the disturbances induced by the step size used in increasing the buoyancy ratio. Both structures are dynamically equivalent and are named S3. The flow pattern S3 has also been identified in a stratified fluid layer in a magnetic field, with periodic and free boundary conditions on the vertical and horizontal boundaries, respectively (Rucklidge *et al.* 2000). However, this structure is stable in a very limited range and at $Ra^* = 12$ it undergoes a pitchfork bifurcation to the two-dimensional structure S34, having $Z_2 \times O_2$ symmetry, where the diagonal plane symmetries s_d and $s_{d'}$ are broken. As Ra^* is increased, structure S34 bifurcates to structure S36, having $Z_2 \times Z_2 \times O_2$ symmetry and then to structure S30 having a single diagonal plane symmetry $\{e, s_d\} = Z_2$. At a higher thermal Rayleigh number, S30 bifurcates to either structure S5 having D_{4h} symmetry, or to S10 having D_{2h} symmetry.

Structure S31 with a single diagonal symmetry $s_{d'}$, has the maximum Sherwood number at the highest thermal Rayleigh number investigated. However this structure is unstable for $Ra^* < 100$ and as Ra^* is decreased from 100 to 90 it evolves to non-symmetric structures S38 and S39. Depending on the time step used in the simulations, it may also evolve to structure S32 having a plane and a translational symmetry along the x-direction, ($Z_2 \times Z_2$ symmetry), or to structure S18 having Z_2 symmetry. At this Rayleigh number, the non-symmetric structure S38 contains very small-amplitude (1.5% of the average) periodic oscillations of average Sherwood number, but becomes steady at $Ra^* = 80$ and 70 and evolves to structure S5 having D_{4h} symmetry as Ra^* is further decreased to 60. However, this structure is unstable

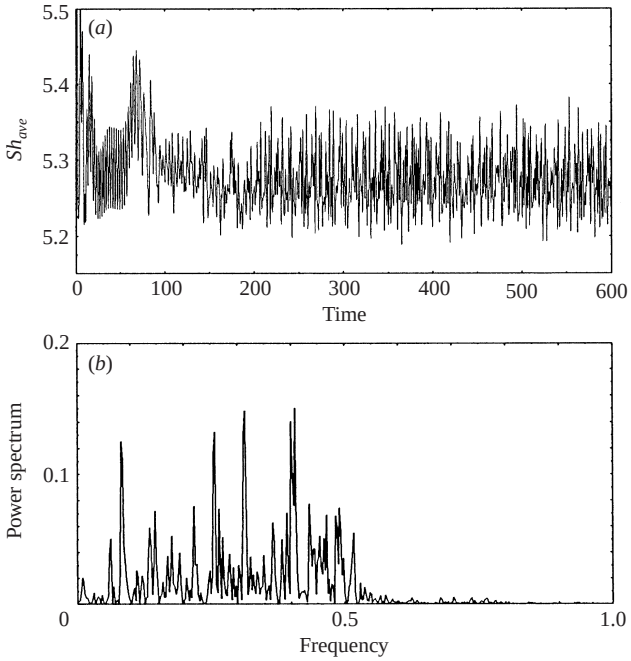

FIGURE 7. Same as figure 6 except for $N = 3.5$.

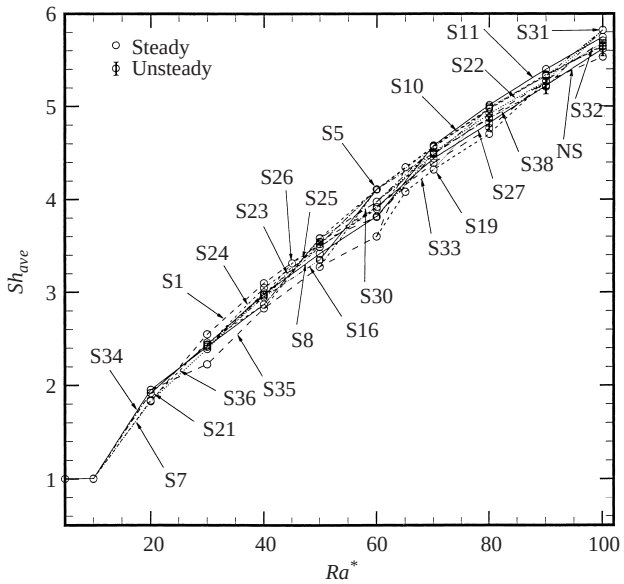

FIGURE 8. Variations of average Sherwood number with porous thermal Rayleigh number. $N = 0.5$; $Le = 10$.

at lower Rayleigh numbers and evolves to a non-symmetric structure, when Ra^* is decreased from 60 to 50.

It is interesting that for increasing thermal Rayleigh number all transitions are to a higher branch of solutions, where the average Sherwood number is higher. Based on this observation we might think that the evolution of the flow structures is such

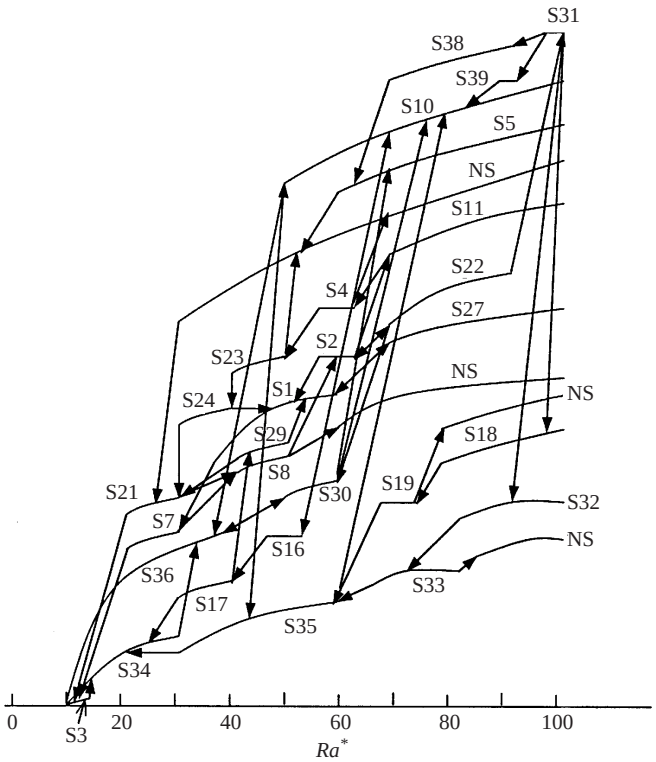

FIGURE 9. Schematic diagram of the flow transitions as a function of porous thermal Rayleigh number.

that the convective system adopts the configuration that maximizes solute transport. A similar argument was put forward by Malkus (1954) that the flow will evolve to a steady configuration that maximizes the heat transport. However, the results of Straus & Schubert (1979) on three-dimensional convection in a porous cavity heated from below with no double diffusive effects and that of Graham & Steen (1994) on two-dimensional convection in a porous cavity, do not support the maximal heat transport idea. They found solutions where the Nusselt number can actually decrease with increasing Rayleigh number. A similar observation was made in this study on solute transport for decreasing Ra^*, where the transitions are expected to proceed towards lower solution branches in the Sh versus Ra^* diagram. A counter example to this is found for the transition of non-symmetric structure S39. When Ra^* is decreased from 90 to 80, structure S39 evolves to structure S10 which is on a higher solution branch, corresponding to higher average Sherwood numbers.

Structure S1 with D_4 symmetry has the maximum average Sherwood number between $30 \leqslant Ra^* \leqslant 50$. At higher porous thermal Rayleigh numbers, structure S11 with $D_2 \times Z_2 = D_{2h}$ symmetry has the maximum average Sherwood number until $Ra^* = 90$ and at $Ra^* = 100$ structure S31 takes over. The average Nusselt number is close to unity and varies between 1.0 and 1.12 for all thermal Rayleigh numbers investigated, indicating a diffusion-dominated heat transfer. Structures S30, S10, S31, S5, S33, S18 and S19 are all similar, differing only by the number of rolls. Structures having a smaller number of rolls are generally stable at lower Ra^* values, with the region of stability shifting to higher Ra^* values as the number of rolls increases.

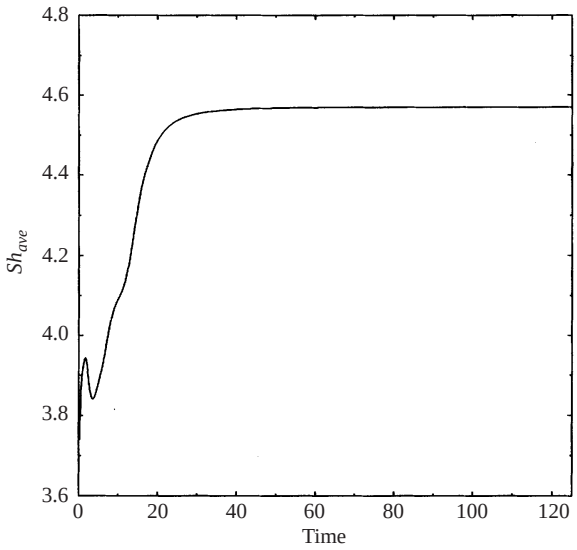

FIGURE 10. Time variation of the average Sherwood number during transition from structure S35 to S10. $Ra^* = -70$; $N = -0.5$; $Le = 10$.

The two-dimensional four-roll structure S35 has the least mass transfer capacity among all structures in the range $30 \leqslant Ra^* \leqslant 60$, as reflected by the low Sh_{ave} values in figure 8. However, this is not a rule for two-dimensional structures. For example, the two-dimensional two-roll structure S34 has the highest Sh_{ave} value among all structures at $Ra^* = 20$. On the other hand, at a higher Ra^* value of 30 the three-dimensional structure S1 has a higher average Sherwood number than S34. The structure having the maximum solute transport capacity may be either two-dimensional or three-dimensional depending on the thermal Rayleigh number range. A similar behaviour exists for heat transfer in the case of pure Rayleigh–Bénard convection in a porous cubic enclosure (Straus & Schubert 1979). Also, it has been found that steady two-dimensional patterns are stable at rather low thermal Rayleigh numbers, and, for $Ra^* > 60$, all structures are three-dimensional.

When Ra^* is increased from 60 to 70, the two-dimensional structure S35 bifurcates to the three-dimensional structure S10. The variation of the average Sherwood number during transition from S35 to S10 is shown in figure 10. The snapshots of flowlines on different planes and isolines of T, C and $\mathrm{d}C/\mathrm{d}t$ during this transition are illustrated in figure 11. The original flow pattern consists of two-dimensional roll cells whose axes of rotation are parallel to the y-axis. At the initial stages of the bifurcation process, dipole vortices start forming at the top and bottom of the transverse plane, as observed from projection of flow lines on the (y, z)-plane at $X = 0.8$. The driving mechanism of this process is the local variation in the concentration field. The contour plot of the rate of change of the concentration field at the bottom row at $t = 4$ shows that alternating positive and negative variations in the concentration of the fluid occur at locations of the dipole vortices. The fluid in the high concentration regions tends to rise upward, opposing the main flow direction as a result of which a dipolar vortex structure forms. The vortices grow in size and eventually transform into toroidal roll cells. The isotherms are almost parallel to the horizontal axis indicating that the temperature field remain almost unaffected by the flow during this process so that the heat transfer is purely conductive. On the other hand, solute

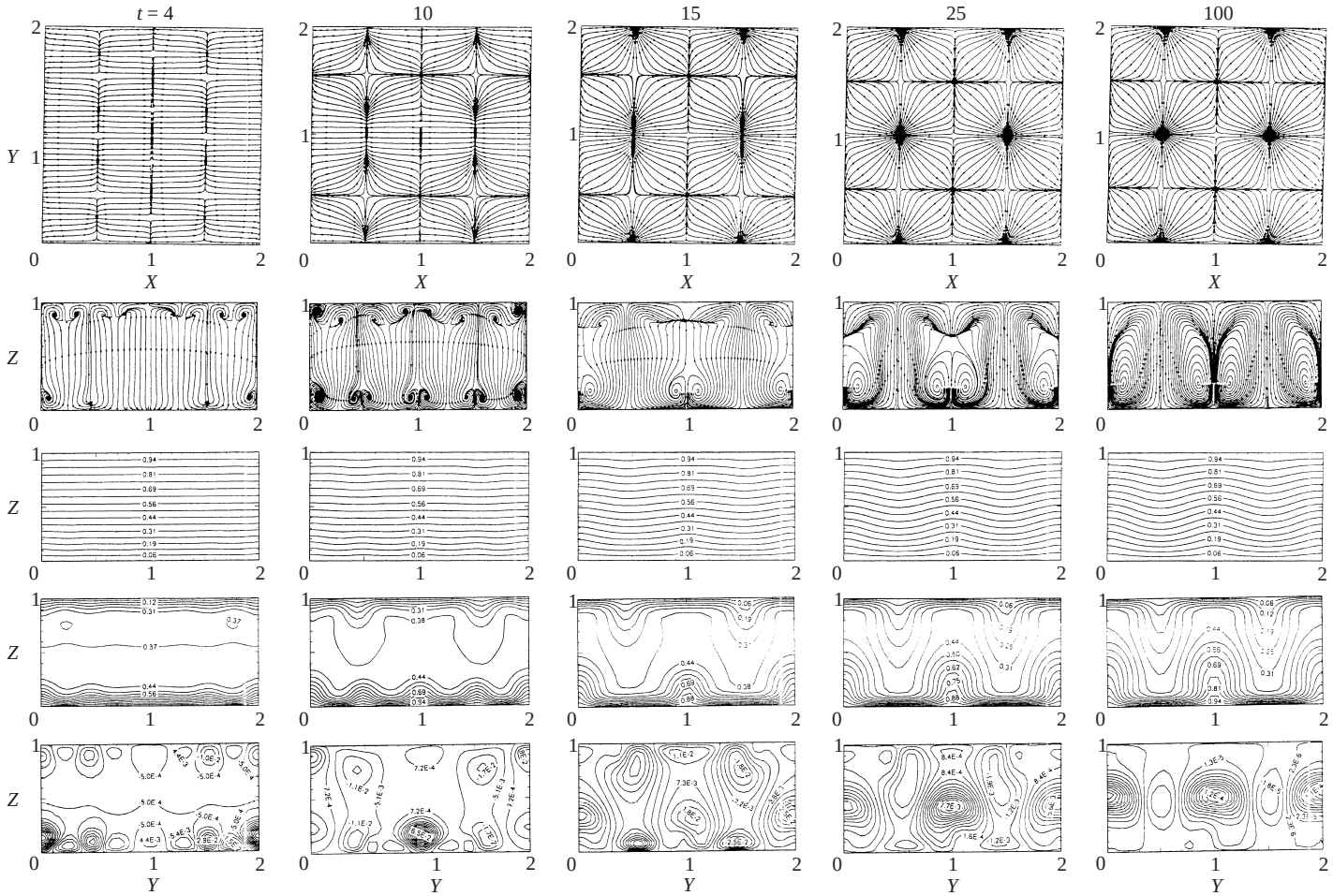

FIGURE 11. Evolution of the three-dimensional flow structure S10 from the two-dimensional structure S35. Top row: projection of flow lines on the horizontal plane at $Z = 0.9$; second row: projection of flow lines on (y, z)-plane at $X = 0.8$; third row: isotherms on (y, z)-plane at $X = 0.8$; fourth row: isoconcentration lines on (y, z)-plane at $X = 0.8$; fifth row: isoclines of $\mathrm{d}C/\mathrm{d}t$ on (y, z)-plane at $X = 0.8$.

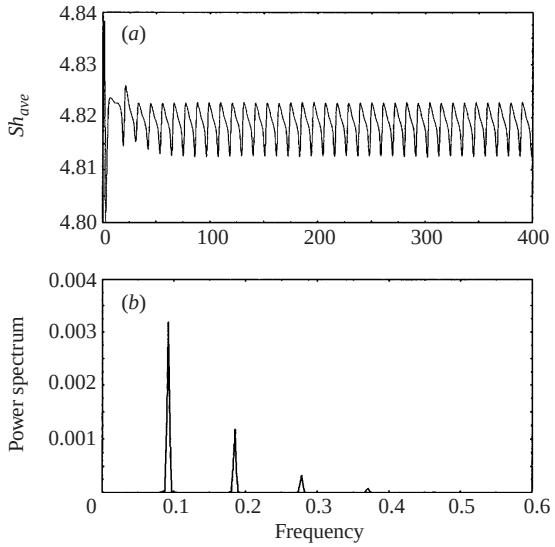

FIGURE 12. (*a*) Time variation of the average Sherwood number and (*b*) the power spectra of its deviation from the time mean value for $Ra^* = 80$, starting from the steady flow structure S27 at $Ra^* = 70$ ($N = 0.5$, $Le = 10$).

transport is mainly by convection since species diffusion is negligible at high Lewis numbers.

Structure S1 having $\{e, s_x, s_y, s_d, s_{d'}, r, r^2, r^3\} = D_4$ symmetry undergoes a pitchfork bifurcation to structure S27 when Ra^* is increased from 60 to 70, where six of its symmetries are broken with only the $\{e, s_d\} = Z_2$ being retained. Small-amplitude oscillations are set in the basic flow when Ra^* is increased to 80 of which the temporal variation of the average Sherwood number together with its power spectra are given in figure 12. The amplitude of oscillations is about 0.2% of the average value. The flow is periodic with a dominant frequency of 0.0927 and its harmonics. Reversion back to steady flow occurs as Ra^* is increased further to 90, with solution at $Ra^* = 80$ as the initial conditions. The convective patterns starts becoming unsteady again as Ra^* is increased further to 100 using the solution at $Ra^* = 90$ as the initial condition. The oscillations of the average Sherwood number are less than 0.1% of the average, as observed from figure 13. The power spectrum of the deviation of Sh_{ave} from its time mean value indicates that the oscillations are periodic with a dominant frequency of 0.0264 and a very small-amplitude harmonic, which is barely noticeable with the scale used.

4.1.5. *Effect of Lewis number*

Variation of average Sherwood number with Lewis number is illustrated in figure 14 for $N = 0.5$ and $Ra^* = 5$. The bifurcation diagram is constructed by changing the Lewis number in steps of 10, where the solution obtained is used as the initial condition for the next run. The average Nusselt number is close to unity and varies between 1.0 and 1.002 in the Lewis number range investigated, which points to a diffusive heat transfer. The flow transitions as a function of Lewis number are shown in figure 15. Starting with the diffusive solution as initial conditions, convection starts at $60 < Le < 70$, with the resulting two-dimensional two-roll structure S34. However, convection was found to persist down to $Le \approx 20$ when Lewis number is decreased

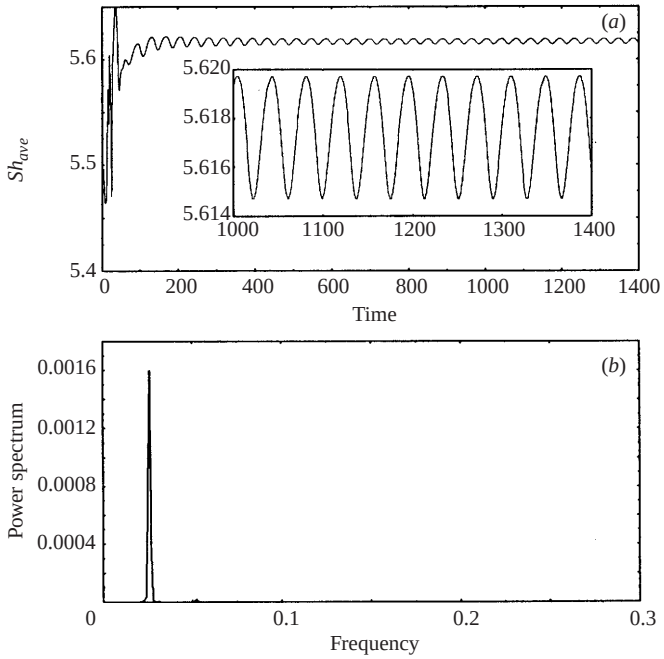

FIGURE 13. (*a*) Time variation of the average Sherwood number and (*b*) the power spectra of its deviation from the time mean value for $Ra^* = 100$, starting from the steady flow structure S27 at $Ra^* = 90$ ($N = 0.5$, $Le = 10$).

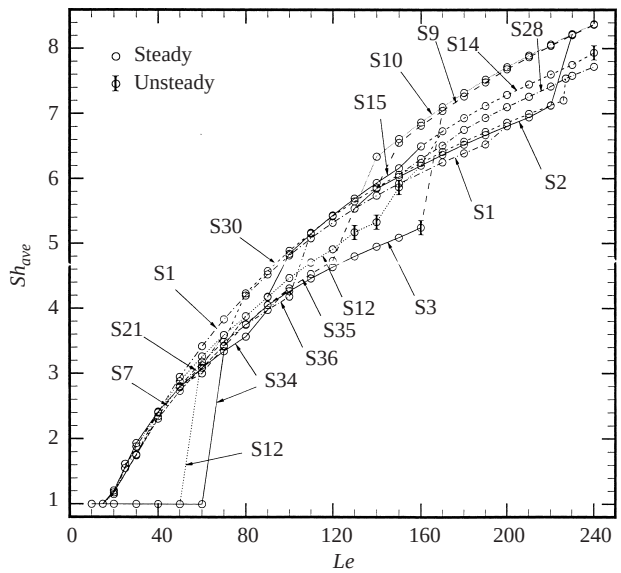

FIGURE 14. Variations of average Sherwood number with Lewis number. $Ra^* = 5.0$; $N = 0.5$.

in steps using the results obtained at the higher Lewis numbers, indicating that the transition from the diffusive to the convective regime is subcritical. As a result, several modes exist simultaneously below the onset threshold of convective motion. Structures S34, S3 and S21 are found to exist below the threshold, which pass to a diffusive state when *Le* is lowered below about 20.

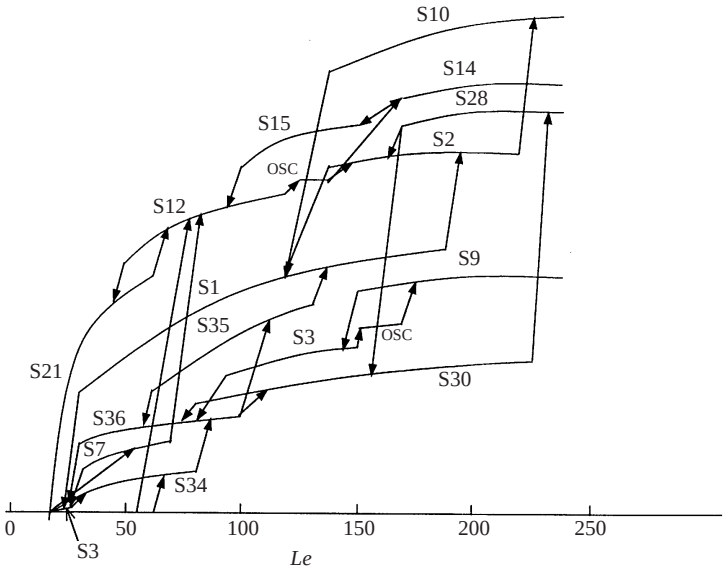

FIGURE 15. Schematic diagram of the flow transitions as a function of Lewis number.

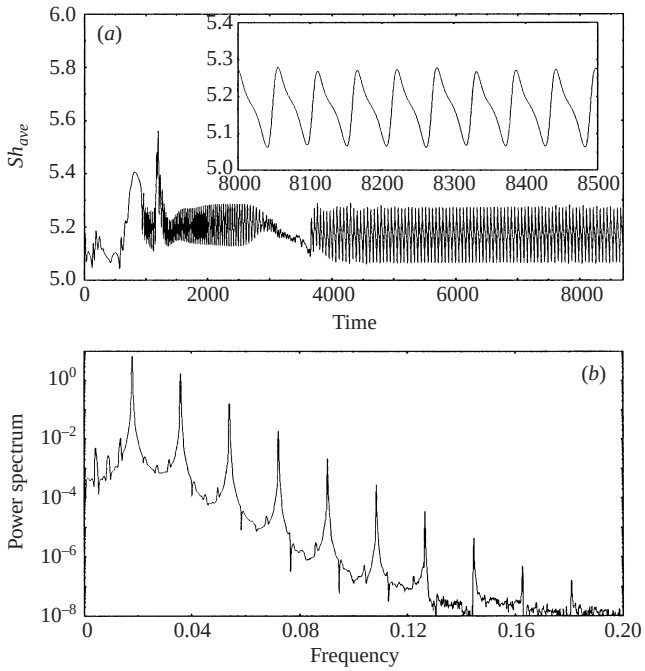

FIGURE 16. (*a*) Time variation of the average Sherwood number and (*b*) the power spectra of its deviation from the time mean value for $Le = 130$, starting from the steady flow structure S12 at $Le = 120$ ($N = 0.5$, $Ra^{*} = 5$).

Starting with the two-roll structure S34 having $Z_2 \times O_2$ symmetry and increasing the Lewis number results in the three-roll structure S36 with $D_2 \times O_2$ symmetry. This structure then bifurcates to Z_2-symmetric structure S30 as Le is increased further. When Le is increased from 226 to 227, a new structure, S28, is obtained from S30 as a result of splitting of its largest and its smallest cells, where the diagonal symmetry

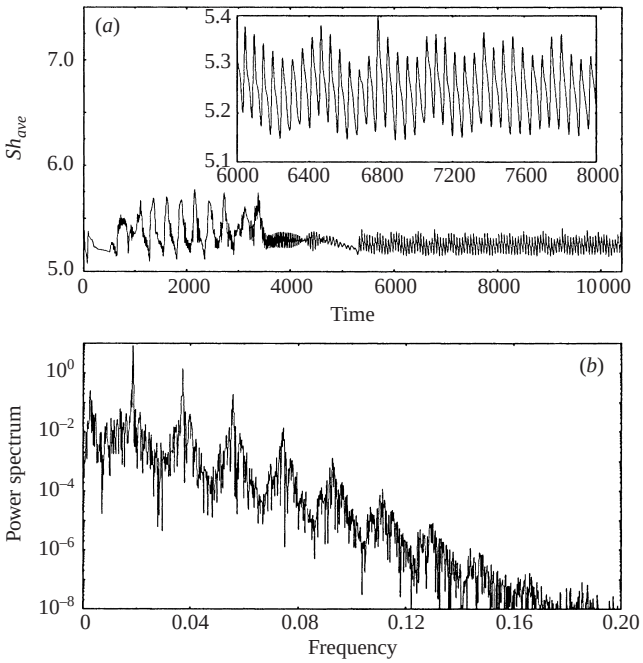

FIGURE 17. As figure 16 except $Le = 135$.

is preserved. Another branch of solutions follow the path where S36 first bifurcates to the four-roll structure S35 by gaining a translational symmetry in the y-direction with the resulting symmetry group $D_2 \times O_2$ then to D_4-symmetric structures S1 and S2 and finally to D_{2h}-symmetric pattern S10 as Le is increased further. However, using a stabilizing linear temperature gradient with zero concentration and velocity profiles as initial conditions, convection starts at a Lewis number between 50 and 60, with the resulting flow structure S12 having Z_2 symmetry. This structure is steady up to $Le = 120$ and oscillations set in at higher Lewis numbers. For $Le = 130$, oscillations are periodic as revealed from the power spectrum of the average Sherwood number at the bottom plate (figure 16). The spectrum consists of a main frequency of 0.018 and its harmonics. The oscillation amplitude of the average Sherwood number is only about 4% of the mean. At a Lewis number of 135, small-amplitude oscillations are superimposed on the periodic waveform as revealed from the power spectrum shown in figure 17. For $Le = 140$, the oscillations amplitude is about the same as shown in figure 18. However, the power spectrum consists of many frequencies with a main frequency of 0.0196. At a Lewis number of 150, the amplitude of oscillations reach to about 12% of the mean and the main frequency decreases to 0.00259, as shown in figure 19. At a Lewis number of 160, the flow resumes back to the D_4-symmetric steady-flow structure S2 or to S14, having plane symmetry $\{e, s_x\} = Z_2$ with three main and four smaller uprising plumes. This steady flow structure is stable up to $Le = 240$ where oscillations start. Structure S14 bifurcates to another Z_2-symmetric structure, S15, with merging of its two smaller rolls as Lewis number is decreased from 160 to 150. This branch then follows the path with Z_2 symmetric patterns S12, S21 and finally to a diffusive state as Le is decreased further.

The toroidal roll structure S3, with D_4 symmetry, is stable in two different Lewis number ranges at steady state. One is close to the convective threshold ($Le = 20$),

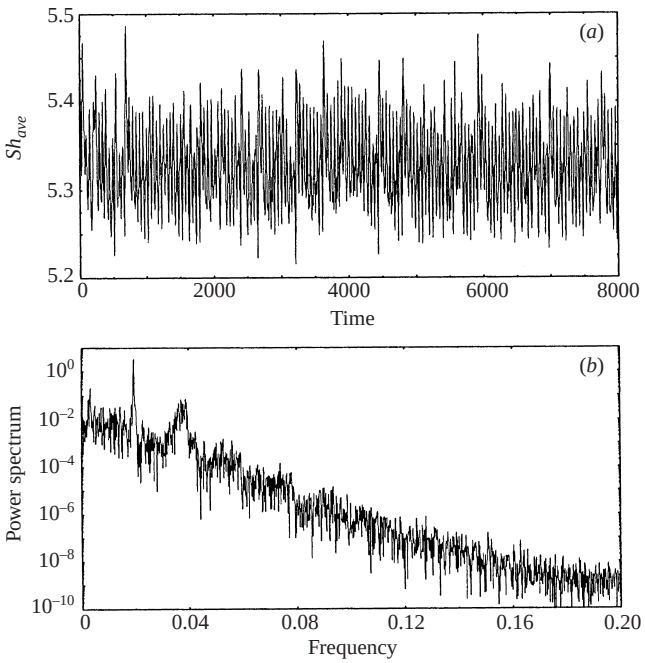

FIGURE 18. As figure 16 except $Le = 140$.

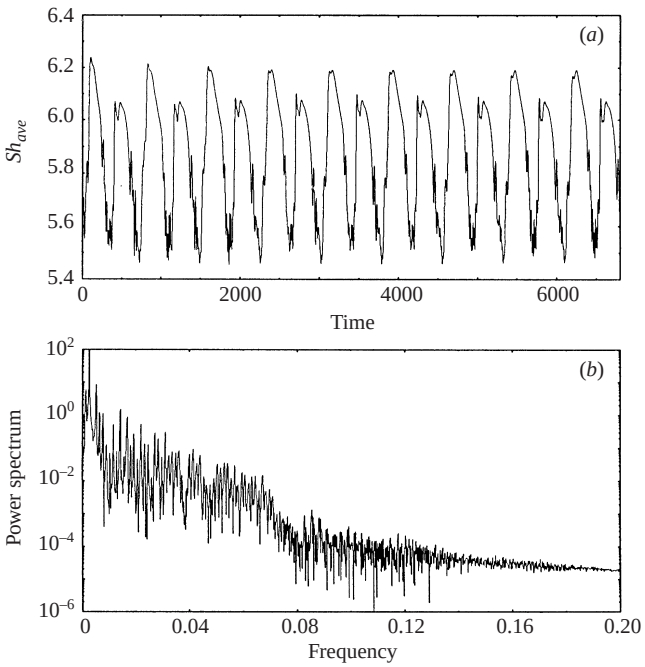

FIGURE 19. As figure 16 except $Le = 150$.

where it bifurcates to the two-dimensional pattern S34 having $Z_2 \times O_2$ symmetry. The other range of stability of S3 is between $Le = 90$ and 150, which is obtained by abruptly increasing the Lewis number to 100 from the diffusive state. At lower Lewis numbers it evolves to two-dimensional three-roll structure S36 having $D_2 \times O_2$ symmetry. As the Lewis number is increased from 150 to 160, structure S3 undergoes

a Hopf bifurcation to a periodic state having a frequency of 0.0859 and at $Le = 170$ it bifurcates to D_2 symmetric steady flow structure S9 by losing its plane and rotational symmetries but retaining the diagonal symmetries s_d and $s_{d'}$.

Structure S10, with D_{2h} symmetry, has the highest mass transfer capability at high Lewis numbers and is obtained from the bifurcation of D_4-symmetric pattern S2 when Le is increased from 220 to 230. However, this structure loses its stability for $Le < 140$ and bifurcates to S1 having D_4 symmetry. Structure S1 is stable over a wide range of Lewis numbers; namely for $30 \leqslant Le \leqslant 190$, where it evolves to S2 at the high end and to S3 at the lower end of the Lewis number range through transcritical bifurcations, where its D_4 symmetry is preserved in both cases. Structure S30, which has a single diagonal symmetry, $\{e, s_d\} = Z_2$, also exists over a large range of Lewis numbers ($80 \leqslant Le \leqslant 226$). It evolves to S28 having Z_2 symmetry and S36 having $D_2 \times O_2$ symmetry at the higher and lower Lewis numbers, respectively. The occurrence of other structures is limited to a narrower range of Lewis numbers.

5. Conclusions

The onset of multiple three-dimensional double-diffusive flow patterns in a horizontal rectangular porous cavity with opposing gradients of temperature and concentration in the fingering regime, where the solute gradient is destabilizing against a stabilizing temperature gradient has been investigated numerically. Altogether 36 symmetric steady-flow structures have been identified and the transitions between the solution branches determined for changes in buoyancy ratio, thermal Rayleigh number and Lewis number.

Simulations were carried out starting with the diffusive solution and increasing the related parameter to a point beyond which unsteady flow starts. However, structures S12, S3 and S27 have been found to exhibit unsteady behaviour in some part of the ranges investigated, whereas all other structures are steady. The three-roll structure S12, having Z_2 symmetry, follows the route steady, periodic, quasi-periodic, chaotic and eventually evolves to the steady four-roll structure S30 or S2 as the buoyancy ratio varies in the range 2 to 4, for $Ra^* = 0.5$ and $Le = 10$. A similar behaviour is observed for the same structure when the Lewis number is increased in steps of 10. However, this time, the quasi-periodic state has not been detected in the above sequence of transitions, possibly because of the large Lewis number intervals used. On the other hand, the bifurcation sequence of structure S27 involves only steady periodic, and then returns back to the original steady flow regime of the same structure, as Ra^* is changed in the range 60–90, for $Le = 10$ and $N = 0.5$.

When increasing buoyancy ratio, thermal Rayleigh number or Lewis number, all transitions are to a higher branch of solutions, where the average Sherwood number is higher. On the other hand, when decreasing any of the variables, the transitions are to a lower solution branch. An exception to this behaviour occurs for the transition of the non-symmetric structure S39. When Ra^* is decreased from 90 to 80, structure S39 evolves to S10, which is on a higher solution branch, with higher average Sherwood numbers. As a result, it is not possible to put forward a general statement saying that the flow structures adopt the configuration, which maximize solute transport. The Nusselt number is close to unity ($1 \leqslant Nu \leqslant 1.3$) for all the parameters investigated, indicating a diffusion-dominated heat transfer.

No single structure was found to exist for all the buoyancy ratio, thermal Rayleigh number or Lewis numbers investigated. However, structures S30, S1 and S10 have

been found to exist in a relatively wider range of parameters and they have the maximum mass transfer capacity. The occurrence of other structures is limited to narrower ranges.

REFERENCES

Anderson, D. M. & Worster, M. G. 1995 Weakly nonlinear analysis of convection in mushy layers during the solidification of binary alloys. *J. Fluid Mech.* **302**, 307–331.

Armstrong, M. A. 1988 *Groups and Symmetry*. Springer.

Chen, F. & Chen, C. F. 1993 Double-diffusive fingering convection in a porous medium. *Intl J. Heat Mass Transfer* **30**, 793–807.

Emms, P. W. & Fowler, A. C. 1994 Compositional convection in the solidification of binary alloys. *J. Fluid Mech.* **262**, 111–139.

Ergun, S. 1952 Fluid flow through packed column. *Chem. Engng Prog.* **48**, 89–94.

Gollub, J. P. & Benson, S. V. 1980 Many routes to turbulent convection. *J. Fluid Mech.* **100**, 449–470.

Graham, M. D. & Steen, P. H. 1994 Plume formation and resonant bifurcations in porous-media convection. *J. Fluid Mech.* **272**, 67–89.

Griffiths, R. W. 1981 Layered double diffusive convection in a porous media. *J. Fluid Mech.* **102**, 221–248.

Hackbush, W. 1994 *Iterative Solution of Large Sparse System of Equations*. Springer.

Hortmann, M., Peric, M. & Scheuerer, G. 1990 Finite volume multigrid prediction of laminar natural convection: bench-mark solutions. *Intl J. Numer. Meth. Fluids* **11**, 189–207.

Imhoff, P. T. & Green, T. 1988 Experimental investigation of double-diffusive groundwater fingers. *J. Fluid Mech.* **188**, 363–382.

Karimi-Fard, M., Charrier-Mojtabi, M. C. & Mojtabi, A. 1999 Onset of stationary and oscillatory convection in a tilted porous cavity saturated with a binary fluid: linear stability analysis. *Phys. Fluids* **11**, 1346–1358.

Kimura, S., Schubert, G. & Straus, J. M. 1986 Time dependent convection in a fluid-saturated porous cube heated from below. *J. Fluid Mech.* **207**, 153–189.

Lauriat, G. & Prasad, V. 1989 Non-Darcian effects on natural convection in a vertical porous enclosure. *Intl J. Heat Mass Transfer* **32**, 2135–2148.

Leonard, B. P. & Mokhtari, S. 1990 Beyond first order upwinding: the ULTRA-SHARP alternative for nonoscillatory steady-state simulation of convection. *Intl J. Numer. Meth. Engng* **30**, 729–766.

Malashetty, M. S. 1993 Anisotropic thermoconvective effects on the onset of double diffusive convection in a porous medium. *Intl J. Heat Mass Transfer* **36**, 2397–2401.

Malkus, W. V. R. 1954 The heat transport and spectrum of thermal turbulence. *Proc. R. Soc. Lond.* A **225**, 196–212.

Mamou, M., Vasseur, P. & Bilgen, P. 1998 A Galerkin finite element study of the onset of double-diffusive convection in an inclined porous enclosure. *Intl J. Heat Mass Transfer* **41**, 1513–1529.

Mamou, M. & Vasseur, P. 1999 Thermosolutal bifurcation phenomena in porous enclosures subject to vertical temperature and concentration gradients. *J. Fluid Mech.* **395**, 61–87.

Murray, B. T. & Chen, C. F. 1989 Double-diffusive convection in a porous medium. *J. Fluid Mech.* **201**, 147–166.

Nield, D. A. 1968 Onset of thermohaline convection in a porous medium. *Water Resources Res.* **4**, 553–560.

Nield, D. A., Manole, D. M. & Lage, J. L. 1993 Convection induced by inclined thermal and solutal gradients in a shallow horizontal layer of a porous medium. *J. Fluid Mech.* **257**, 559–574.

Patil, P. R. & Rudriah, N. 1980 Linear convective instability and thermal diffusion of a horizontal quiescent layer of a two component fluid in a porous medium. *Intl J. Engng Sci.* **18**, 1055–1059.

Rosenberg, N. D. & Spera, F. J. 1992 Thermohaline convection in a porous medium heated from below. *Intl J. Heat Mass Transfer* **35**, 1261–1273.

Rubin, H. 1973 Effect of nonlinear stabilizing salinity profiles on thermal convection in a porous medium layer. *Water Resources Res.* **9**, 211–221.

Rubin, H. 1976 Onset of thermohaline convection in a cavernous aquifer. *Water Resources Res.* **12**, 141–147.

Rucklidge, A. M., Weiss, N. O., Brownjohn, D. P., Matthews, P. C. & Proctor, M. R. E. 2000 Compressible magnetoconvection in three dimensions: pattern formation in a strongly stratified layer. *J. Fluid Mech.* **419**, 283–323.

Rudraiah, N. & Malashetty, M. S. 1986 The influence of coupled molecular diffusion on double diffusive convection in a porous medium. *J. Heat Transfer* **108**, 872–876.

Sezai, I. & Mohamad, A. A. 1999 Three-dimensional double-diffusive convection in a porous cubic enclosure due to opposing gradients of temperature and concentration. *J. Fluid Mech.* **400**, 333–353.

Sezai, I. & Mohamad, A. A. 2000 Natural convection in a rectangular cavity heated from below and cooled from top as well as the sides. *Phys. Fluids* **12**, 432–443.

Shyy, W. & Sun, C. S. 1993 Development of a pressure-correction staggered-grid based multigrid solver for incompressible recirculating flows. *Comput. Fluids* **22**, 51–76.

Stone, H. L. 1968 Iterative solution of implicit approximations of multi-dimensional partial differential equations. *SIAM J. Numer. Anal.* **5**, 530–558.

Straus, J. M. & Schubert, G. 1979 Three-dimensional convection in a cubic box of fluid-saturated porous material. *J. Fluid Mech.* **91**, 155–165.

Taslim, M. E. & Narusawa, U. 1986 Binary fluid convection and double-diffusive convection in a porous medium. *J. Heat Transfer* **108**, 221–224.

Taunton, J. W. & Lightfoot, E. N. 1972 Thermohaline instability and salt fingers in a porous medium. *Phys. Fluids* **15**, 748–753.

Trevisan, O. V. & Bejan, A. 1987 Mass and heat transfer by high Rayleigh number convection in a porous medium heated from below. *Intl J. Heat Mass Transfer* **30**, 2341–2356.

Tyvand, P. D. 1980 Thermohaline instability in anisotropic porous media. *Water Resources Res.* **16**, 325–330.

Vafai, K. & Kim, S. J. 1995 On the limitations of the Brinkman–Forchheimer-extended Darcy equation. *Intl J. Heat Fluid Flow* **16**, 11–15.

Van der Vorst, H. A. 1992 BiCGSTAB: A fast and smoothly converging variant of Bi-CG for the solution of non-symmetric linear systems. *SIAM J. Sci. Statist. Comput.* **13**, 631–644.

Van Doormaal, J. P. & Raithby, G. D. 1984 Enhancements of the simple method for predicting incompressible fluid flows. *Numer. Heat Transfer Fluid Flow* **7**, 147–163.

Worster, G. 1986 Solidification of an alloy from a cooled boundary. *J. Fluid Mech.* **167**, 481–501.

Zhao, C., Mühlhaus, H. B. & Hobbs, B. E. 1998 Effects of geological inhomogeneity on high Rayleigh number steady state heat and mass transfer in fluid saturated porous media heated from below. *Numer. Heat Transfer* A **33**, 415–431.